



HAL
open science

Study of the Sextans dwarf spheroidal galaxy from the DART Ca ii triplet survey

G. Battaglia, E. Tolstoy, A. Helmi, M. Irwin, P. Parisi, V. Hill, P. Jablonka

► **To cite this version:**

G. Battaglia, E. Tolstoy, A. Helmi, M. Irwin, P. Parisi, et al.. Study of the Sextans dwarf spheroidal galaxy from the DART Ca ii triplet survey. Monthly Notices of the Royal Astronomical Society, 2011, 411, Issue 2, pp.1013-1034. 10.1111/j.1365-2966.2010.17745.x . hal-00632628

HAL Id: hal-00632628

<https://hal.science/hal-00632628>

Submitted on 17 Sep 2021

HAL is a multi-disciplinary open access archive for the deposit and dissemination of scientific research documents, whether they are published or not. The documents may come from teaching and research institutions in France or abroad, or from public or private research centers.

L'archive ouverte pluridisciplinaire **HAL**, est destinée au dépôt et à la diffusion de documents scientifiques de niveau recherche, publiés ou non, émanant des établissements d'enseignement et de recherche français ou étrangers, des laboratoires publics ou privés.



Distributed under a Creative Commons Attribution 4.0 International License

Study of the Sextans dwarf spheroidal galaxy from the DART Ca II triplet survey[★]

G. Battaglia,^{1†} E. Tolstoy,² A. Helmi,² M. Irwin,³ P. Parisi,⁴ V. Hill⁵ and P. Jablonka⁶

¹European Organization for Astronomical Research in the Southern Hemisphere, K. Schwarzschild-Str. 2, 85748 Garching, Germany

²Kapteyn Astronomical Institute, University of Groningen, PO Box 800, 9700 AV Groningen, the Netherlands

³Institute of Astronomy, Madingley Road, Cambridge CB03 0HA

⁴INAF – Istituto di Astrofisica Spaziale e Fisica Cosmica di Bologna, via Gobetti 101, 40129 Bologna, Italy

⁵Université de Nice Sophia-Antipolis, CNRS, Observatoire de la Côte d'Azur, Laboratoire Cassiopée, B.P. 4229, 06304 Nice cedex 4, France

⁶Observatoire de Genève, Laboratoire d'Astrophysique de l'Ecole Polytechnique Fédérale de Lausanne (EPFL), CH-1290 Sauverny, Switzerland

Accepted 2010 September 17. Received 2010 September 6; in original form 2010 June 25

ABSTRACT

We use Very Large Telescope (VLT)/Fibre Large Array Multi Element Spectrograph (FLAMES) intermediate-resolution ($R \sim 6500$) spectra of individual red giant branch stars in the near-infrared Ca II triplet (CaT) region to investigate the wide-area metallicity properties and internal kinematics of the Sextans dwarf spheroidal galaxy (dSph). Our final sample consists of 174 probable members of Sextans with accurate line-of-sight velocities ($\pm 2 \text{ km s}^{-1}$) and CaT [Fe/H] measurements ($\pm 0.2 \text{ dex}$). We use the Mg I line at 8806.8 \AA as an empirical discriminator for distinguishing between probable members of the dSph (giant stars) and probable Galactic contaminants (dwarf stars). Sextans shows a similar chemodynamical behaviour to other Milky Way dSphs, with its central regions being more metal rich than the outer parts and with the more metal-rich stars displaying colder kinematics than the more metal-poor stars. Hints of a velocity gradient are found along the projected major axis and along an axis at position angle (PA) = 191° , however, a larger and more spatially extended sample may be necessary to pin down the amplitude and direction of this gradient. We detect a cold kinematic substructure at the centre of Sextans, consistent with being the remnant of a disrupted very metal poor stellar cluster. We derive the most extended line-of-sight velocity dispersion profile for Sextans, out to a projected radius of 1.6 . From Jeans modelling of the observed line-of-sight velocity dispersion profile we find that this is consistent with both a cored dark matter halo with large core radius and cuspy halo with low concentration. The mass within the last measured point is in the range $2\text{--}4 \times 10^8 M_\odot$, giving very large mass-to-light ratios, from 460 to $920 (M/L)_{V,\odot}$.

Key words: stars: abundances – galaxies: dwarf – galaxies: individual: Sextans dSph – galaxies: kinematics and dynamics – Local Group – dark matter.

1 INTRODUCTION

The Sextans dwarf spheroidal galaxy (dSph) is a satellite of the Milky Way (MW; heliocentric distance of 86 kpc from Irwin et al. 1990; Mateo, Fischer & Krzemiński 1995; 95.5 kpc from Lee et al. 2003). Sextans was discovered relatively recently by automatic scanning of APM plates by Irwin et al. (1990). This is because the Sextans dSph (hereafter Sextans) is one of the most diffuse and faint dSphs, with a central surface brightness $\Sigma_0 = 18.2 \pm$

$0.5 \text{ mag arcmin}^{-2}$ and luminosity $L = 4.1 \pm 1.9 \times 10^5 L_\odot$ (Irwin & Hatzidimitriou 1995). This, together with its location on the sky ($l = 243.5$, $b = +42.3$ from Mateo 1998), results in a considerable amount of contamination from MW stars. This makes it particularly difficult to explore the two-dimensional (2D) structure of Sextans and search for possible asymmetries or other features (Irwin & Hatzidimitriou 1995).

A further difficulty in the study of Sextans is given by its large extent on the sky ($r_{\text{core}} = 16.6 \pm 1.2 \text{ arcmin}$; $r_{\text{tidal}} = 160.0 \pm 50 \text{ arcmin}$ from Irwin & Hatzidimitriou 1995, see also Table 1), which is not well suited to the field of view of most current wide area imagers and spectrographs. Several imaging studies of the central region (at most the inner $40 \times 40 \text{ arcmin}^2$) of Sextans (Mateo et al. 1991, 1995; Bellazzini, Ferraro & Pancino 2001; Harbeck et al. 2001; Lee et al.

[★]Based on FLAMES observations collected at the ESO, proposal 171.B-0588.

[†]E-mail: gbattagl@eso.org

Table 1. The various rows are from top to bottom: coordinates of the optical centre; position angle, defined as the angle between the north direction and the major axis of the galaxy measured counter-clockwise; ellipticity, defined as $e = 1 - b/a$; King core and tidal radius; exponential radius; systemic velocity in the heliocentric and in the GSR system; global velocity dispersion, in the heliocentric and in the GSR system; distance modulus and heliocentric distance; luminosity in V band (based on the apparent magnitude measured by Irwin & Hatzidimitriou 1995 but readjusted for a distance of 86 kpc by Łokas 2009); V magnitude of the horizontal branch; reddening.

Parameter	Value	Reference
$(\alpha_{J2000}, \delta_{J2000})$	$10^{\text{h}}13^{\text{m}}03^{\text{s}}, -01^{\circ}36'54''$	1
PA	56°	2
e	0.35	2
R_{core}	16.6 arcmin	2
R_{tidal}	160 arcmin	2
R_e	15.5 arcmin	2
v_{sys}	$226.0 \pm 0.6 \text{ km s}^{-1}$	3
$v_{\text{sys,GSR}}$	$78.4 \pm 0.6 \text{ km s}^{-1}$	3
σ	$8.4 \pm 0.4 \text{ km s}^{-1}$	3
σ_{GSR}	$8.4 \pm 0.4 \text{ km s}^{-1}$	3
$(m - M)_0$	19.67	1
Distance	86 kpc	1
L_V	$4.37 \pm 1.69 \times 10^5 L_{\odot}$	2, 4
V_{HB}	20.35	2
$E(B - V)$	0.0477	5

References: 1 = Mateo (1998); 2 = Irwin & Hatzidimitriou (1995); 3 = this work; 4 = Łokas (2009); 5 = Schlegel, Finkbeiner & Davis (1998), <http://irsa.ipac.caltech.edu/cgi-bin/bgServices/nph-bgExec>, average value over 5° .

2003) have shown that the majority of its stars are ancient (> 10 Gyr old), as evidenced by the presence of horizontal branch (HB) and RR Lyrae stars. A significant population of stars have also been found on the main sequence (MS), above the oldest turn-off. It was suggested that these may be MS stars as young as 2 Gyr (e.g. Mateo et al. 1991). However, deep Suprime-Cam V and I photometry at Subaru (Okamoto et al. 2008) shows that their spatial distribution is very similar to old (> 10 Gyr) MS stars below the oldest turn-off, indicating that these are likely to be old blue stragglers (BS) stars (> 10 Gyr) rather than young MS stars (see also Lee et al. 2003).

In common with other dSphs, Sextans presents spatial variations of its stellar population mix, with the red horizontal branch (RHB) stars more centrally concentrated than the blue horizontal branch (BHB) stars (Bellazzini et al. 2001; Harbeck et al. 2001; Lee et al. 2003; Kleyna et al. 2004). By estimating the luminosity difference between the HB and the MS turn-off out to the nominal tidal radius of Sextans, Okamoto et al. (2008) estimate an age difference of at least 3 Gyr between the outer parts (with age ~ 14 Gyr) and the central parts (with age ~ 10 Gyr). The younger stars are more centrally concentrated than the older ones, consistent with the different distribution of RHB and BHB stars. The other populations, red giant branch (RGB), BS and MS stars, have a spatial distribution intermediate to the one of RHB and BHB stars: this indicates that their spatial distribution can be thought of as a combination of the stellar distribution of RHB and BHB stars, i.e. RGB, BS and MS are likely to represent both components.

No determinations have yet been made of the large-scale metallicity properties in Sextans. Spectroscopic estimates of the mean metallicity ($[\text{Fe}/\text{H}]$) of Sextans are available from Ca II triplet (CaT) observations of individual RGB stars in the central regions (< 20 arcmin) of the galaxy (Da Costa et al. 1991, $[\text{Fe}/\text{H}] =$

-1.7 ± 0.25 dex, six stars; Suntzeff et al. 1993, -2.05 ± 0.04 dex, 43 stars), which also revealed an internal $[\text{Fe}/\text{H}]$ spread. High-resolution spectroscopic observations of five RGB stars in Sextans by Shetrone, Côté & Sargent (2001) confirmed both the average $[\text{Fe}/\text{H}]$ found in the CaT studies, and the large range of observed metallicities ($\Delta[\text{Fe}/\text{H}] = 1.4$ dex). The derivation of the mean $[\text{Fe}/\text{H}]$ and spread in Sextans by Geisler & Sarajedini (1996) from Washington photometry is also in agreement with the spectroscopic studies. Recently Aoki et al. (2009) and Tafelmeyer et al. (2010) followed up at high spectral resolution six and two stars in Sextans, respectively, confirming the presence of stars with $[\text{Fe}/\text{H}]$ down to -3.1 .

Studies on the internal kinematics of Sextans have shown that, in common with the other dSphs, this galaxy exhibits a much larger velocity dispersion than what is expected from the gravitational contribution of its luminous matter, hinting at the presence of large amounts of dark matter (DM; Suntzeff et al. 1993; Hargreaves et al. 1994; Kleyna et al. 2004; Walker et al. 2006). The latest estimate (Walker et al. 2007) based on a velocity dispersion profile from 504 members gives a mass of $5.4 \times 10^7 M_{\odot}$ within the last measured point at ~ 65 arcmin (equivalent to ~ 4 core radii, ~ 0.4 tidal radii), i.e. a mass-to-light (M/L) ratio of $130 (M/L)_{\odot}$. Strigari et al. (2007) used a sample of 294 members from Walker et al. (2006) and estimated a mass of $0.9^{+0.4}_{-0.3} \times 10^7 M_{\odot}$ within 0.6 kpc ($13^{+11}_{-5.8} \times 10^7 M_{\odot}$ extrapolated to 4 kpc), which corresponds to an $M/L = 260 (M/L)_{\odot}$. Although the mass estimates are not directly comparable as they refer to different distances from the Sextans centre, they all point to mass-to-light ratios so large as to require considerable amounts of DM, if the hypothesis of dynamical equilibrium holds. These spectroscopic samples do not reach the nominal tidal radius and therefore the masses determined are likely to be lower limits.

With its unusually large extent on the sky and large tidal-to-core radius ratio ($r_{\text{tidal}}/r_{\text{core}} \sim 9.6$ as compared to ratios between 3 and 6 for most of the other classical dSphs; see Irwin & Hatzidimitriou 1995), Sextans seems a natural candidate for tidal disruption. However, no clear signs of disruption such as tidal tails and S-shaped contours have been found in Sextans. This may however just be a consequence of the observational challenge of detecting such signs in a low surface brightness and heavily contaminated object like Sextans, or that such signs are not necessarily expected in tidally disrupted galaxies, as some N -body simulations show (see e.g. Muñoz, Majewski & Johnston 2008). A small velocity gradient has been detected approximately along the projected minor axis of this galaxy by Walker, Mateo & Olszewski (2008). However, given that no proper motions have been directly measured for Sextans, it is unclear whether this gradient is a sign of tidal disruption as predicted, for example, in the models of Oh, Lin & Aarseth (1995), due to geometrical effects (Strigari 2010) or an intrinsic gradient.

In this paper we use a spectroscopic sample of line-of-sight velocities and $[\text{Fe}/\text{H}]$ measurements for 174 RGB stars probable members of Sextans, obtained at Very Large Telescope (VLT)/Fibre Large Array Multi Element Spectrograph (FLAMES), to analyse both the wide-field metallicity properties and the internal kinematics of this galaxy. Our sample extends out to 6 core radii (0.7 times the nominal tidal radius). The structure of the paper is the following. In Section 2 we describe the observations, the data reduction technique and the adopted metallicity scale. In Section 3 we deal with the issue of separating Galactic contaminants from Sextans members and we use the Mg I line as an empirical discriminator between dwarf and giant stars. In Section 4 we present the results from our survey regarding the wide-area metallicity and kinematic properties of Sextans as well as the presence of kinematic substructures. Finally, we

perform a mass determination in Section 5 and present discussion and conclusions in Sections 6 and 7.

2 OBSERVATIONS AND DATA REDUCTION

The spectroscopic observations were carried out at VLT/FLAMES between 2003 and 2004, with the exception of one pointing which was re-observed in 2008 May, during the commissioning of the upgraded Grating Instrument for Radiation Analysis with a Fiber-FedEchelle (GIRAFFE) spectrograph CCD.

For the selection of our spectroscopic targets we used photometric data from Isaac Newton Telescope (INT)/Wide Field Camera (WFC) covering approximately an area of $2^\circ \times 2^\circ$ centred on the coordinates of the optical centre of the galaxy and European Southern Observatory (ESO)/Wide Field Imager (WFI) photometry for 12 pointings spread over the outer regions of the system. The imaging data were reduced following standard procedures, for details see references in Battaglia et al. (2006). In this work these photometric data are used exclusively to select spectroscopic targets.

We selected targets classified as stellar in our photometry and with a position on the colour–magnitude diagram (CMD) consistent with an RGB star, but with a wide colour range to avoid biasing our sample in age or in metallicity.

We used VLT/FLAMES feeding the GIRAFFE spectrograph in Medusa mode, that allows the simultaneous allocation of 132 fibres (including sky fibres) over a 25 arcmin diameter field of view (Pasquini et al. 2002). We used the GIRAFFE low-resolution grating LR8 (resolving power $R \sim 6500$), covering the wavelength range from 8206 to 9400 Å. This allows the measurement of equivalent widths (EW) from the near-infrared CaT lines at 8498, 8542 and 8662 Å and also enables the derivation of velocities accurate to a few km s^{-1} . The spectra used in this work are from 16 different fields in Sextans obtained with this set-up (see Table 2 for the observations journal). These data were reduced using the GIRAFFE pipeline (Geneva Observatory; Blecha et al. 2003).

The sky-subtraction and extraction of the velocities and EWs of CaT lines were carried out using our own software developed by M. Irwin. For the details see Battaglia et al. (2008a). Here we just

note that we estimate the CaT EW in two ways. The first consists in simply summing the flux contained in a region 15 Å wide centred on each CaT line (hereafter integral fit). To derive the second estimate we fit individual unconstrained Gaussian functions to each CaT line over the same wavelength region (hereafter Gaussian fit). The combined EWs for CaT lines #2 and #3 (λ_{8542} , λ_{8662}) for both the integral and Gaussian fits are then compared and used to compute an overall correction to the Gaussian fit. This is necessary since the observed CaT lines have non-Gaussian wings which are progressively more visible as the EW increases.

Beside the EW of the CaT lines, we also measure the EW of a Mg I line at 8806.8 Å. The EW of this line is estimated using the values from the integrated fit, summing the flux contained in a region 6 Å wide centred on the Mg I line. The EW of this line will be used as a discriminant between Sextans stars and MW contaminants as described in Section 3.2.

We observed a total of 1294 targets, which include 103 stars with double measurements, 70 with three measurements, five with four measurements. The number of distinct targets is 1036.

As described in our previous studies using the same instrument and set-up we ensured a high reliability for the data used in our analysis by excluding those stars with signal-to-noise ratio (S/N) per Å < 10 and velocity errors larger than 5 km s^{-1} (e.g. Battaglia et al. 2008a). In order to ensure the reliability of the EW measurements we also required that the summed EW of the two strongest CaT lines should not differ by more than 2 Å between the determination from the integral fit and the Gaussian fit.

Fig. 1 shows the distribution of differences in velocity for the stars that have double measurements (103 objects), both without any selection criteria and adopting the above selection criteria for each measurement (59 objects). Fig. 2 refers to the distribution of differences in summed EW from Gaussian fit of CaT lines and integrated flux for the Mg I line. The determination of the summed CaT EW from the integral and Gaussian estimators yields quite similar distributions, and therefore, for consistency with our previous work, hereafter we use the summed CaT EW derived from the Gaussian estimator. For the EW of the Mg I line the integral estimator yields slightly less noisy measurements and therefore we will use this for

Table 2. Journal of our VLT/FLAMES observations at $R \sim 6500$ of Sextans. The columns give, respectively, the name of the observed field, the coordinates of the FLAMES pointing, the UT date of observation, the exposure time, the median S/N and the number of the observed spectra. All these observations were taken in service mode by ESO staff. Field 102 and ext_14 have repeated exposures because the first exposures did not meet the required criteria for the maximum allowed seeing and/or airmass. These repeated exposures also allow a check for the internal velocity and EWs errors.

Field name	RA (J2000)	Dec. (J2000)	Date	Exp. time (s)	S/N	N_{targ}
Sext_100	10 ^h 12 ^m 58 ^s .1	−01°38′05″.5	2003-12-20	2700	18.6	54
Sext_101	10 ^h 14 ^m 47 ^s .4	−01°11′27″.5	2003-12-22	3800	17.2	55
Sext_102	10 ^h 13 ^m 22 ^s .1	−01°21′53″.6	2004-03-14	500, 1125, 3600	2.9, 4.5, 15.5	74, 92, 92
Sext_103	10 ^h 11 ^m 13 ^s .3	−01°12′01″.9	2003-12-22	4000	13.3	50
Sext_104	10 ^h 11 ^m 21 ^s .6	−01°31′38″.0	2004-03-15	3600	21.1	68
Sext_112	10 ^h 13 ^m 38 ^s .5	−02°00′35″.6	2008-05-25	3600	14.0	81
Sext_113	10 ^h 14 ^m 52 ^s .3	−02°24′24″.5	2004-01-01	3600	25.1	48
Sext_114	10 ^h 12 ^m 24 ^s .1	−01°58′43″.5	2004-03-16	4600	17.5	83
Sext_115	10 ^h 11 ^m 30 ^s .4	−02°09′45″.0	2003-12-20	3600	8.8	57
sext_ext_02	10 ^h 17 ^m 03 ^s .1	−01°01′49″.8	2004-03-17	3600	26.8	76
sext_ext_03	10 ^h 18 ^m 36 ^s .3	−00°24′21″.9	2004-03-18	3600	28.7	69
sext_ext_04	10 ^h 20 ^m 43 ^s .2	−00°06′51″.4	2004-03-19	3600	37.4	79
sext_ext_06	10 ^h 13 ^m 22 ^s .9	−00°26′51″.1	2004-03-20	4200	42.0	68
sext_ext_08	10 ^h 08 ^m 27 ^s .4	−00°52′01″.6	2004-03-17	3600	31.6	58
sext_ext_14	10 ^h 07 ^m 42 ^s .2	−03°13′27″.8	2004-03-20/21	2511, 3600	29.9, 33.3	66, 66
sext_ext_16	10 ^h 07 ^m 29 ^s .2	−01°40′19″.7	2004-03-21	4500	27.7	57

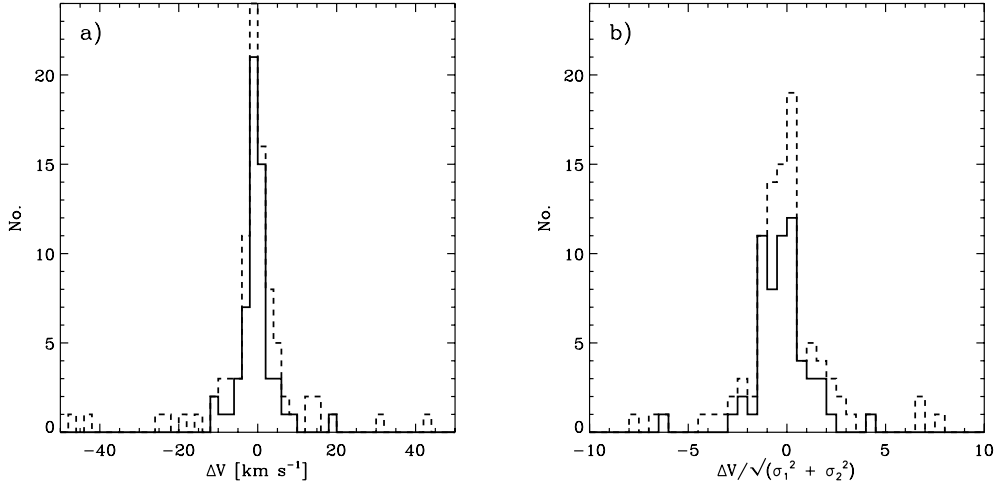


Figure 1. Comparison between velocity measurements for stars with double measurements in the Sextans dSph. (a) Distribution of velocity differences for all the stars (dashed line), and for the stars with S/N per $\text{\AA} \geq 10$ and estimated error in velocity $\leq 5 \text{ km s}^{-1}$ for each measurement (solid line). The weighted mean velocity, rms dispersion and scaled median absolute deviation from the median (where the scaled median absolute deviation from the median (MAD) is $1.48 \times \text{MAD} \equiv$ a robust rms e.g. Hoaglin, Mosteller & Tukey 1983) are 0.9 ± 3.0 , 29.0 ± 2.2 , 4.3 km s^{-1} (dashed line) and -0.6 ± 0.5 , 2.5 ± 0.5 , 2.0 km s^{-1} (solid line). (b) As above but now the velocity difference is normalized by the predicted error. With these S/N and velocity error cuts the measured error in the velocity distribution is close to the expected unit variance Gaussian ($1.48 \times \text{MAD} = 0.98$).

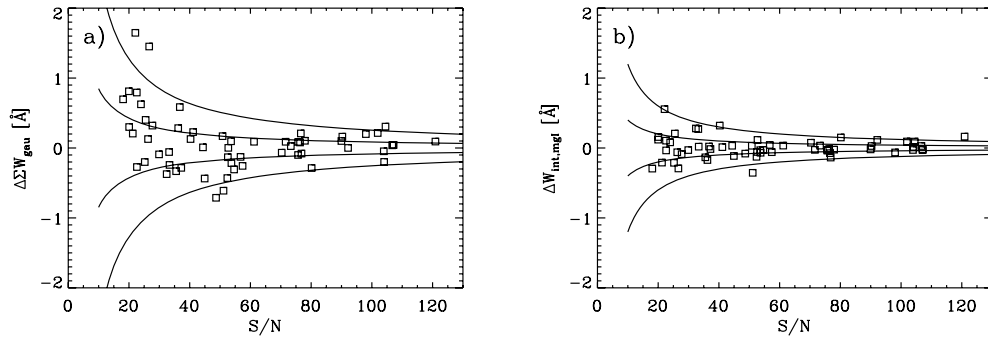


Figure 2. Comparison between EW measurements for stars with double measurements in the Sextans dSph. Distribution of summed CaT EW ($\text{EW}_2 + \text{EW}_3$) differences from Gaussian fit (left) and Mg I EW differences from integrated flux (right) as a function of S/N for the stars with S/N per $\text{\AA} \geq 10$ and estimated error in velocity $\leq 5 \text{ km s}^{-1}$ for each measurement. Assuming a similar S/N for the individual measurements of each star, the error in the summed CaT EW difference is $\sqrt{2} \times \sigma_{\Sigma W} = \sqrt{2} \times 6/(S/N)$ while the error in the Mg I EW difference is $\sqrt{2} \times \sigma_{\Sigma W} = \sqrt{2} \times 2.8/(S/N)$. The solid lines indicate the 1 and 3 σ region for the error in the difference of summed EW. The weighted mean summed CaT EW difference, rms dispersion in the difference and scaled MAD are 0.03 ± 0.05 , 0.22 ± 0.06 and 0.25 \AA . The weighted mean in the Mg I EW difference, rms dispersion and scaled median absolute deviation from the median are $0.01 \pm 0.02 \text{ \AA}$, 0.09 ± 0.03 and 0.08 \AA .

the Mg I line. The error in the summed CaT EW for the individual measurements is given by $\sigma_{\Sigma W} = 6/(S/N)$, while the error in the Mg I EW is well represented by $2.8/(S/N)$.

In the following, when calculating the velocity, summed CaT EW and all the other properties of the stars with repeated measurements, we use only the individual measurements which meet our S/N and velocity errors criteria (before combining them).

The final sample was carefully checked to weed out any spurious objects (e.g. broken fibres, background galaxies, foreground stars, etc.). We removed four objects because they were observed with broken fibres; we found three background galaxies and removed nine objects because the continuum shape or the presence of very broad absorption line was not consistent with what is expected for RGB stars.

Our final sample of acceptable measurements for velocities and CaT EWs consists of 789 stars. We provide a detailed comparison between this data set and the one from Walker, Mateo & Olszewski (2009a) in the appendix.

2.1 Metallicity scale

We use the CaT EWs to derive metallicities ($[\text{Fe}/\text{H}]$) for the target stars.

The near-infrared CaT lines have been extensively used in the literature as empirical estimators of the $[\text{Fe}/\text{H}]$ abundance of individual RGB stars observed at intermediate spectral resolution.

This method has been empirically calibrated for stellar clusters and proven reliable over the range $-2.1 \lesssim [\text{Fe}/\text{H}] \lesssim -0.2$ and $2.5 \lesssim \text{age [Gyr]} \lesssim 13$ (e.g. Rutledge et al. 1997; Cole et al. 2004) on the Carretta & Gratton (1997) metallicity scale. Battaglia et al. (2008a) tested the validity of the method for composite stellar populations, observing the same 129 individual stars in the Sculptor and Fornax dSphs both at intermediate and high resolution, and showed that the CaT EW– $[\text{Fe}/\text{H}]$ relation can be applied to composite stellar populations over the explored range $-2.5 \lesssim [\text{Fe}/\text{H}] \lesssim -0.5$.

Starkenburg et al. (2010) carried out a synthetic spectral analysis of the CaT lines down to $[\text{Fe}/\text{H}] = -4$ in order to understand their

theoretical behaviour as a function of physical parameters such as metallicity, gravity, effective temperature and possible biases in the low metallicity range. The authors find that a simple linear relation no longer holds approximately below $[\text{Fe}/\text{H}] \lesssim -2.5$. This behaviour is mostly a reflection of the change of the CaT lines from wing dominated at high metallicity to core dominated at low metallicity.

The authors provide a revised relation, which holds over the much larger range $-4.0 \lesssim [\text{Fe}/\text{H}] \lesssim -0.5$:

$$[\text{Fe}/\text{H}] = -2.87 + 0.195 \times (V - V_{\text{HB}}) + 0.458 \times \Sigma W - 0.913 \times \Sigma W^{-1.5} + 0.0155 \times \Sigma W \times (V - V_{\text{HB}}). \quad (1)$$

In the above ΣW is the summed EW of the two strongest CaT lines, i.e. $\Sigma W = \text{EW}_2 + \text{EW}_3$, V is the apparent magnitude in V band of the star and V_{HB} is the apparent magnitude in V band of the horizontal branch of the galaxy. For Sextans we use $V_{\text{HB}} = 20.35$ from Irwin & Hatzidimitriou (1995), which is also consistent with our photometry.

Using our sample of 789 stars along the line of sight to Sextans, we find that the $[\text{Fe}/\text{H}]$ values derived using equation (16) in Battaglia et al. (2008a) and equation (1) compare very well down to $[\text{Fe}/\text{H}] = -2$; at lower metallicities, equation (16) from Battaglia et al. (2008a) provides on average a larger $[\text{Fe}/\text{H}]$ value than the revised calibration given by equation (1), e.g. a $[\text{Fe}/\text{H}] \sim -2.4$ with the old calibration corresponds to approximately $[\text{Fe}/\text{H}] \sim -2.6$ with the revised one and $[\text{Fe}/\text{H}] \sim -2.6$ to about $[\text{Fe}/\text{H}] \sim -3.0$.

In the following we will use equation (1) for our CaT $[\text{Fe}/\text{H}]$ determinations. In order to derive the errors in $[\text{Fe}/\text{H}]$, we follow the approach of Starkenburg et al. (2010), i.e. we consider that the error due to the photometry is negligible with respect to the error in the determination of the CaT EW and we input in equation (1) the values of $\Sigma W - 1\sigma_{\Sigma W}$ and $\Sigma W + 1\sigma_{\Sigma W}$ and derive the corresponding 1σ lower and upper limit in $[\text{Fe}/\text{H}]$. This reflects the fact that the relation is not linear and therefore symmetric errors in the EW determination can translate into asymmetric errors in $[\text{Fe}/\text{H}]$.

3 MEMBERSHIP

Given the low surface brightness of Sextans and its location on the sky, the RGB locus of Sextans is heavily contaminated by MW stars which are located along the line of sight to Sextans. In order to study the metallicity and kinematic properties of Sextans it is important that we first weed out these Galactic interlopers from our sample. These interlopers will be mostly foreground MW stars. Given the Galactic coordinates of Sextans, the Besançon model (Robin et al. 2003) predicts that the majority of interlopers along the line of sight to Sextans is made of dwarf stars, mostly from the thin and thick disc, and by smaller fraction by subgiants and giant stars.

Ideally one would like a method allowing a direct discrimination between members of the dSph (which have been selected to be RGB stars) from non-members (mostly dwarf stars) on the basis of, for example, spectral features indicating physical characteristics, such as in this case gravity. However, no such spectral features have been identified in previous studies using a similar spectral range and set-up. The common approach is therefore statistical.

The simplest way of discerning between members and non-members is to consider the line-of-sight velocity distribution of the observed targets (see Fig. 3 for the distribution of heliocentric velocities for our VLT/FLAMES targets) and iteratively apply a $k\sigma$ cut around the systemic velocity of the galaxy, where σ is the internal line-of-sight velocity dispersion of the galaxy. The $k\sigma$ cut

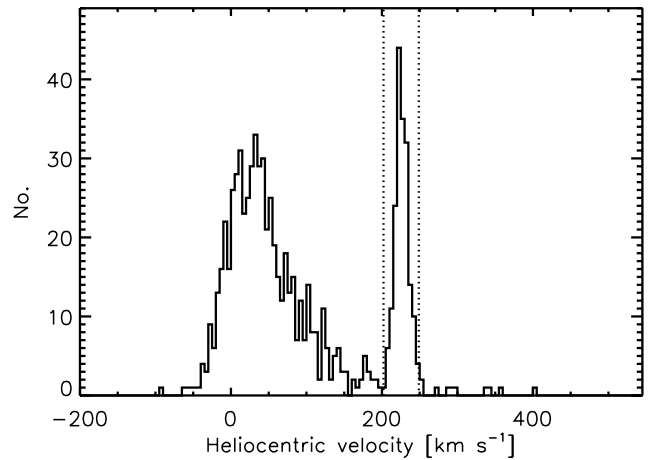


Figure 3. Distribution of heliocentric velocities for the stars observed with VLT/FLAMES in the direction of Sextans and that met our selection criteria. The dotted lines indicate the region used for the 3σ membership selection.

in common use is the 3σ cut, justified by the close to Gaussian line-of-sight velocity distribution observed for dSphs.

We first follow this approach and then refine our selection using further criteria.

3.1 3σ clipping

We first identify the peak of the velocity distribution and derive the weighted average velocity and dispersion for the stars with a velocity within 4σ of the peak, using as a first guess a broad dispersion of $\sigma = 15 \text{ km s}^{-1}$. We then repeat the procedure restricting the range of selection to 3σ . We then apply to the distribution of line-of-sight velocities for the stars within the 3σ range the maximum likelihood method outlined in Hargreaves et al. (1994). This results in a systemic velocity $v_{\text{sys, hel}} = 226.3 \pm 0.6 \text{ km s}^{-1}$ and a global dispersion $\sigma_{\text{hel}} = 8.8 \pm 0.4 \text{ km s}^{-1}$ for 182 probable members. The systemic velocity derived is in very good agreement with the value of $v_{\text{sys, hel}} = 225.8 \pm 0.5 \text{ km s}^{-1}$ from Walker et al. (2006); for the global dispersion they quote values from three sample sizes: $N = 276$, $\sigma_{\text{hel}} = 7.1 \pm 0.3 \text{ km s}^{-1}$; $N = 294$, $\sigma_{\text{hel}} = 8.9 \pm 0.4 \text{ km s}^{-1}$; $N = 303$, $\sigma_{\text{hel}} = 10.3 \pm 0.5 \text{ km s}^{-1}$. Our determination is in very good agreement with their determination from the $N = 294$ sample. We find a good agreement also with the values derived by Hargreaves et al. (1994) ($v_{\text{sys, hel}} = 224.4 \pm 1.6 \text{ km s}^{-1}$, $\sigma_{\text{hel}} = 7.0^{+1.3}_{-1.0} \text{ km s}^{-1}$ from 21 members), and consistent values also to the study of Suntzeff et al. (1993) ($v_{\text{sys, hel}} = 227.9 \pm 1.8 \text{ km s}^{-1}$; $\sigma_{\text{hel}} = 6.2 \pm 0.9 \text{ km s}^{-1}$ based on 33 stars).

Given the large extent on the sky of Sextans, the solar motion and local standard of rest (LSR) will contribute a component along the line of sight to the object, which may introduce spurious velocity gradients and affect the derivation of quantities such as internal rotation for example. In order to remove this effect we transform the heliocentric line-of-sight velocities into line-of-sight velocities in a frame at rest with respect to the Galactic centre (v_{GSR} , where GSR stands for Galactic standard of rest). For this we use the formula in Binney & Tremaine (1987), using a LSR velocity $v_{\text{LSR}} = 220 \text{ km s}^{-1}$ at the solar radius ($R_{\odot} = 8 \text{ kpc}$) and a solar motion of $(U, V, W) = (10, 5.25, 7.17) \text{ km s}^{-1}$ (Dehnen & Binney 1998), where U is radially inward, V positive in the direction of Galactic rotation and W towards the North Galactic Pole.

We repeat the determination of the systemic velocity and global dispersion using the GSR velocities, and we obtain

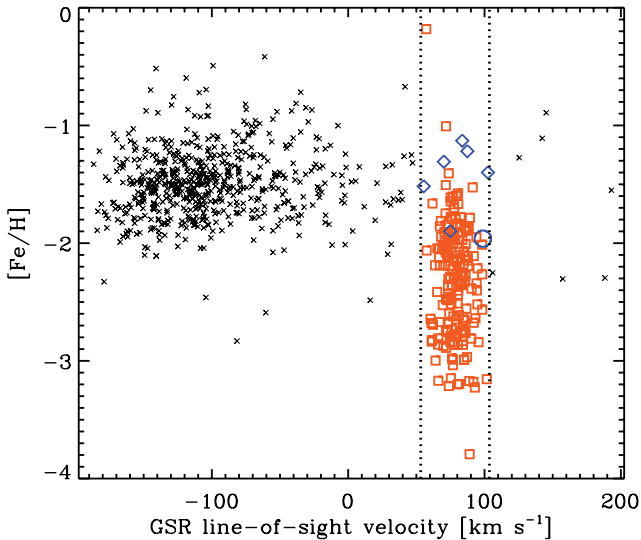


Figure 4. $[\text{Fe}/\text{H}]$ versus GSR line-of-sight velocity for the observed VLT/FLAMES targets (crosses and squares show the stars outside and within the 3σ membership region, respectively; the vertical dotted lines show the velocity membership region). Note that the stars found outside the 3σ membership region, which are probable Galactic contaminants, tend to be preferentially found in the range $-2.0 \lesssim [\text{Fe}/\text{H}] \lesssim -0.5$. This means that Sextans stars at $[\text{Fe}/\text{H}] \lesssim -2.0$ are less likely to be contaminated by Galactic stars whose velocity falls in the 3σ membership selection region. The diamonds indicate stars with velocity consistent with membership but with Mg I EW too large for giant stars (see text). The circle indicates one object with velocity and Mg I EW consistent with membership but with unusual position on the CMD (see text).

$v_{\text{sys,GSR}} = 78.6 \pm 0.7 \text{ km s}^{-1}$ and $\sigma_{\text{GSR}} = 8.8 \pm 0.5 \text{ km s}^{-1}$ for 182 probable members. Here after we will use the GSR velocities, except when comparing the individual line-of-sight velocities from this study to those from other studies to ease the comparison.

3.2 Use of the Mg I line at 8806.8 \AA as a dwarf/giant discriminator

Fig. 4 shows the distribution of $[\text{Fe}/\text{H}]$ measurements for targets along the line of sight to Sextans against their line-of-sight velocity in the GSR system.¹ Around the systemic velocity of Sextans $\pm 3\sigma_{\text{GSR}}$ one can distinguish the stars that are probable members of the galaxy, from those likely to be foreground/background MW stars. From Fig. 4 it is clear that a simple kinematic selection like the 3σ clipping is able to remove the majority of the MW contaminants but that a small fraction may still be present in the 3σ region of membership selection. The fraction of contaminants appears to change with the $[\text{Fe}/\text{H}]$ value derived from the CaT lines: at $[\text{Fe}/\text{H}] \lesssim -2.0$ no considerable contamination is expected, while at larger metallicities Sextans stars are more likely to be contaminated by Galactic stars whose velocity falls in the 3σ membership selection region.

¹ Note that the CaT relation relies on the assumption that all the stars can be considered at the same distance. While this is a reasonable assumption for the stars belonging to the Sextans dSph, this is most likely not the case for the foreground/background MW stars. Therefore, the $[\text{Fe}/\text{H}]$ values for the stars which are probable non-members cannot be considered as meaningful.

Here we attempt a new empirical approach to refine our membership determination, using the Mg I line at 8806.8 \AA as a further possible discriminator between MW and Sextans members.

We first select the stars that have a high probability of membership to Sextans by restricting the velocity range of selection to $2\sigma_{\text{GSR}}$ just for the purpose of this analysis; the highly likely non-members are chosen to be the ones with GSR velocity more than $4\sigma_{\text{GSR}}$ away from Sextans systemic velocity. Given the small EW of the Mg I line, in general less than 1 \AA , only spectra with $\text{S/N per \AA} > 20$ are used to explore possible trends without being affected considerably by the noise. In order to explore the behaviour of the Mg I line with gravity in an empirical way, in Fig. 5 we show the behaviour of the EW of the Mg I line versus the CaT ΣW in bins of V magnitude, for both high likely members and non-members.

As it is visible in Fig. 5 the loci of Mg I EW are quite distinct for members and non-members: members cluster at EW between ~ 0 and 0.2 \AA , while non-members occupy preferably the region of Mg I EW between 0.5 and 0.9 \AA . Some members have negative Mg I EW : this is just a reflection of the lower S/N of those spectra; considering the error bars these are consistent with Mg I EW close to zero, therefore with the line being hidden in the noise.

It is clear that in general the non-members display a larger Mg I EW with respect to members. Preliminary use of synthetic stellar models suggest that this difference may not be driven exclusively by gravity but also of the different metallicity of the dSph star and MW stars (with the former being below $[\text{Fe}/\text{H}] < -1$ and the latter peaking around -0.5 to ~ 0).

From the figure it appears that the trend of Mg I EW versus CaT ΣW changes slightly among the bins in V magnitude, which on a first approximation indicates a dependence on the gravity. However, a safe selection is to consider as members the stars with $\text{Mg I EW} < 0.5 \text{ \AA}$. Hereafter we add this constrain to our selection criteria for probable Sextans stars. We have checked that this selection is valid also when exploring the behaviour of the Mg I EW versus CaT ΣW in bins of $V - I$, as a proxy for effective temperature.

Applying this selection, six stars classified as members from the 3σ clipping appear to be contaminants (these are indicated as diamonds in Fig. 4).

We will improve on the simple empirical approach presented in this section using synthetic spectral libraries in order to assess the applicability range of this method.

3.3 Location on the CMD

Our VLT/FLAMES targets have been chosen to have magnitudes and colours broadly consistent with that expected for RGB stars. We can now apply the membership criteria of the previous two sections to redefine the RGB locus occupied by probable Sextans members. Fig. 6 shows the location on the CMD of the probable members and probable non-members, selected using the criteria of Sections 3.1 and 3.2. All the probable members are closely located along the RGB ridge. The only evident outlier is found at $V - I \sim 0.9$ and $V \sim 17.2$ (see Fig. 6). This star is located at a projected distance $R \sim 2.2$. Given its metallicity of $[\text{Fe}/\text{H}] = -1.9$, its location on the CMD appears inconsistent with stellar evolution models; we therefore exclude this star from subsequent analysis.

3.4 Final sample of probable members

By adopting all the membership criteria described above, i.e. 3σ velocity clipping, Mg I EW and location on the CMD, the final

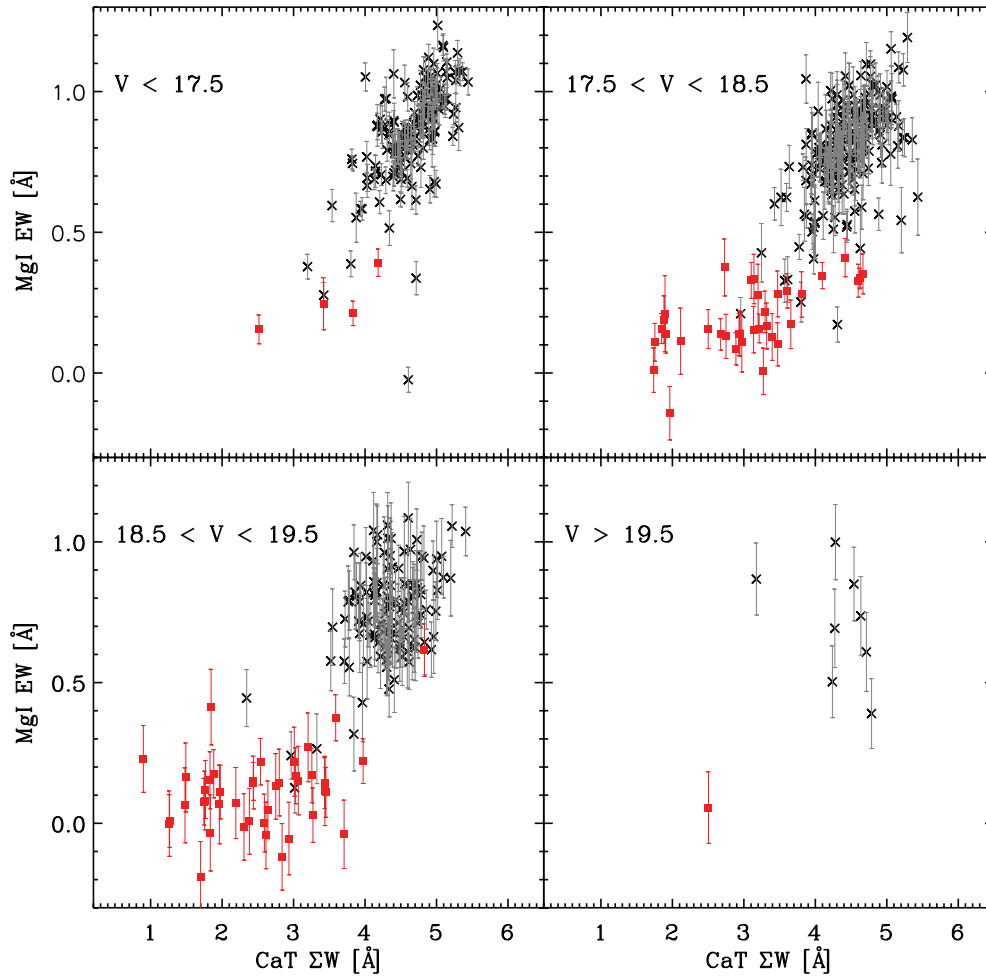


Figure 5. Mg I EW versus CaT ΣW in bins of V magnitude. The range of magnitudes is indicated on the top left-hand corner of the panels. The filled red squares show the stars which are highly probable Sextans members (i.e. with velocities within $\pm 2\sigma$ from the systemic velocity of Sextans) and the open black squares the stars which are highly likely to be MW contaminants (i.e. with velocities at least 4σ away from the systemic velocity of Sextans).

sample of probable members is 174 stars. We have also excluded one star having an error in $[\text{Fe}/\text{H}] > 1$ dex. Using this sample the systemic velocity and global dispersion in the GSR system are $v_{\text{sys,GSR}} = 78.4 \pm 0.6 \text{ km s}^{-1}$ and $\sigma_{\text{GSR}} = 8.4 \pm 0.4 \text{ km s}^{-1}$, while in the heliocentric system they are $v_{\text{sys,hel}} = 226.0 \pm 0.6 \text{ km s}^{-1}$ and a global dispersion $\sigma_{\text{hel}} = 8.4 \pm 0.4 \text{ km s}^{-1}$, all in good agreement with previous determinations. Hereafter we will use this sample for the analysis of the properties of Sextans. The relevant data are listed in Table 3. The location on the field of view of the cleaned up sample and the contaminants is shown in Fig. 7. From this plot the problems in collecting large samples of individual stars in an object like Sextans are clear: it is much extended, therefore many pointings of wide-field area spectrographs like FLAMES are needed, and because of its very low surface brightness, the outermost three pointings did not yield any probable members.

4 RESULTS

4.1 Metallicity properties

Metallicity measurements of large numbers of individual stars are important since they can shed light on the processes that drive galactic chemical enrichment and by measuring the metal abundance in

stars over a wide age range and across the galaxy one can recover how the metal content built up in time and how the enrichment proceeded throughout the galaxy.

Fig. 8 shows the metallicity distribution of probable members of Sextans as derived from our VLT/FLAMES data (left: as a function of elliptical radius; right: overall distribution). The stars in Sextans cover a wide range of $[\text{Fe}/\text{H}]$ values, with the majority covering values from about -3.2 to -1.4 , but reaching down to -3.8 and up to -0.1 ; the average value of the distribution is $[\text{Fe}/\text{H}]_{\text{avg}} = -1.9$, with a scatter of 0.6 dex, and the median value is $[\text{Fe}/\text{H}]_{\text{med}} = -2.3$.

The left-hand panel of Fig. 8 clearly shows that the metallicity properties of this galaxy change with the projected radius from the centre: the inner parts of the galaxy are more metal rich than the outer parts. This kind of behaviour is not unique to Sextans but has been detected also in other MW satellites, on the basis of CaT data. However, here in Sextans the behaviour is more enhanced than in the other systems, with a step-like behaviour of the metallicity distribution going from the region at $R < 0.8$ to the region at $R > 0.8$: while the inner parts ($R < 0.8$) show a broad distribution, covering the whole range of $[\text{Fe}/\text{H}]$ values, the stars in the outer parts ($R > 0.8$) appear to have all $[\text{Fe}/\text{H}]$ values < -2.2 (except for two stars out of 19). The current data appear to suggest a $[\text{Fe}/\text{H}]$ threshold ($[\text{Fe}/\text{H}] = -2.2$) in the

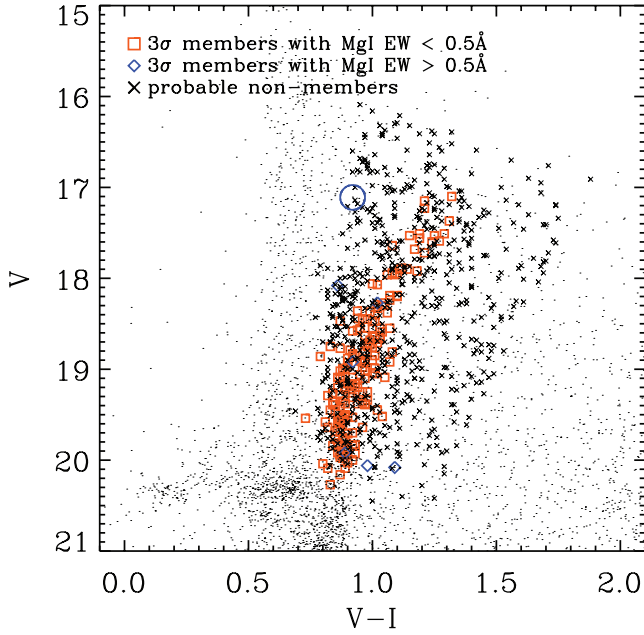


Figure 6. CMD of stellar objects for Sextans as obtained from INT/WFC and ESO/WFI imaging data (dots), with overlaid the targets of our VLT/FLAMES spectroscopic observations which passed our quality criteria. The squares indicate the probable Sextans members, the diamonds the stars that would have been classified as members from the 3σ clipping but that have a too large Mg I EW ($>0.5 \text{ \AA}$), the crosses indicate the stars with velocities outside the 3σ range of selection. The star encircled has a discrepant location on the CMD with respect to the other Sextans members of all metallicities, and it is the outermost star in our sample with a projected radius of more than 2° from Sextans centre. We believe that this star is likely to be a contaminant as well.

outer parts, but more data would be required to confirm that this result is not due to small number statistics.

It is likely that the two ‘metal-rich’ stars at $R > 0:8$ are contaminants: their $[\text{Fe}/\text{H}]$ value is very discrepant with respect to the rest of the distribution, with metallicities of about 1 dex above the largest $[\text{Fe}/\text{H}]$ of the rest of the stars. These stars may be RGB stars belonging to the stellar halo of our Galaxy. Similarly, at $R \sim 0:5$, one star is present with $[\text{Fe}/\text{H}] \sim -0.1$, more than 1 dex larger than the maximum $[\text{Fe}/\text{H}]$ displayed by all the other probable Sextans members anywhere in the galaxy. Even though it is possible that

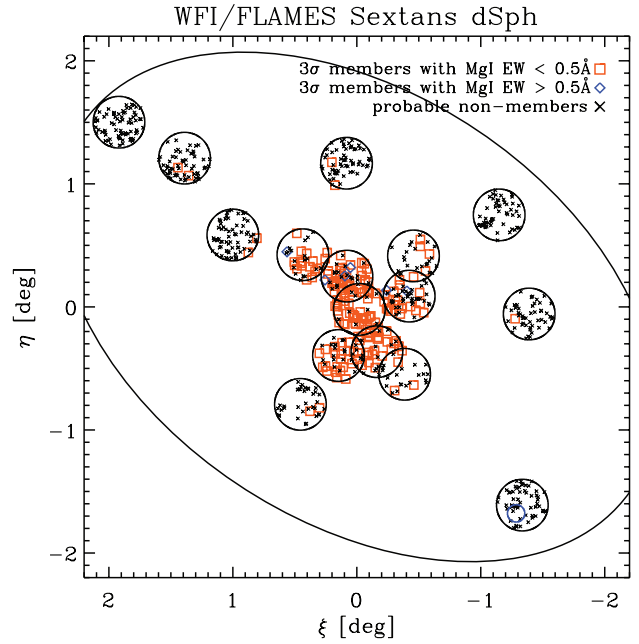


Figure 7. Location of the observed VLT/FLAMES fields (solid circles) and targets in Sextans (squares: probable members; diamonds: stars with velocities within the 3σ range of selection but with too large Mg I EW for giant stars; crosses: non-members with velocities outside the 3σ range of selection). The small blue circle indicates the star with peculiar location on the CMD. The ellipse shows the nominal tidal radius (value from Irwin & Hatzidimitriou 1995).

these three stars may belong to the stellar halo of the MW, these objects full-fill all our membership criteria and we have no means to distinguish them in a direct way from genuine Sextans members, therefore, we will keep them in the analysis.

As shown in Fig. 9 the metallicity distribution of $R > 0:8$ is well approximated by a Gaussian with best-fitting peak position at $[\text{Fe}/\text{H}] = -2.73 \pm 0.06$ and dispersion 0.24 ± 0.05 dex (reduced $\chi^2 = 0.6$). The same figure shows that the region at $R < 0:8$ is well represented by a sum of two Gaussians: one having the same shape parameters – modulo the amplitude – as in the outer parts, and the other Gaussian with best-fitting peak position at $[\text{Fe}/\text{H}] = -2.04 \pm 0.03$ and dispersion 0.25 ± 0.03 dex (reduced $\chi^2 = 0.7$). At $R < 0:8$ these two Gaussians do overlap over a metallicity range and at $[\text{Fe}/\text{H}] \sim -2.3$ the contribution of the stars belonging to the

Table 3. Relevant data for the stars in Sextans observed with VLT/FLAMES that passed our membership criteria. The columns indicate (1) the star ID; (2), (3) star coordinates (right ascension in hours and declination in degrees); (4) S/N per \AA ; (5) heliocentric velocity and its error; (6) summed CaT equivalent width ($\text{EW}_2 + \text{EW}_3$) and its error; (7) $[\text{Fe}/\text{H}]$ value and error, derived adopting the calibration from Starkenburg et al. (2010). The full version of the table is available with the electronic version of the article – see Supporting Information.

Name	α_{J2000}	δ_{J2000}	S/N	v_{hel} (km s^{-1})	ΣW (\AA)	$[\text{Fe}/\text{H}]$
sext_001	10 12 40.27	-1 29 7.7	13.0	241.51 ± 4.64	2.28 ± 0.46	$-2.34^{+0.27}_{-0.31}$
sext_002	10 12 47.98	-1 29 38.8	22.7	222.51 ± 1.70	3.44 ± 0.26	$-1.78^{+0.13}_{-0.13}$
sext_003	10 12 39.03	-1 29 59.0	34.6	235.84 ± 1.22	3.81 ± 0.17	$-1.87^{+0.08}_{-0.08}$
sext_004	10 13 9.94	-1 29 34.9	21.7	241.29 ± 2.81	2.93 ± 0.28	$-1.95^{+0.15}_{-0.15}$
sext_005	10 13 18.97	-1 26 58.2	20.0	216.48 ± 2.40	1.96 ± 0.30	$-2.53^{+0.20}_{-0.23}$
sext_006	10 13 17.14	-1 26 38.1	22.9	245.40 ± 1.48	2.54 ± 0.26	$-2.27^{+0.14}_{-0.15}$

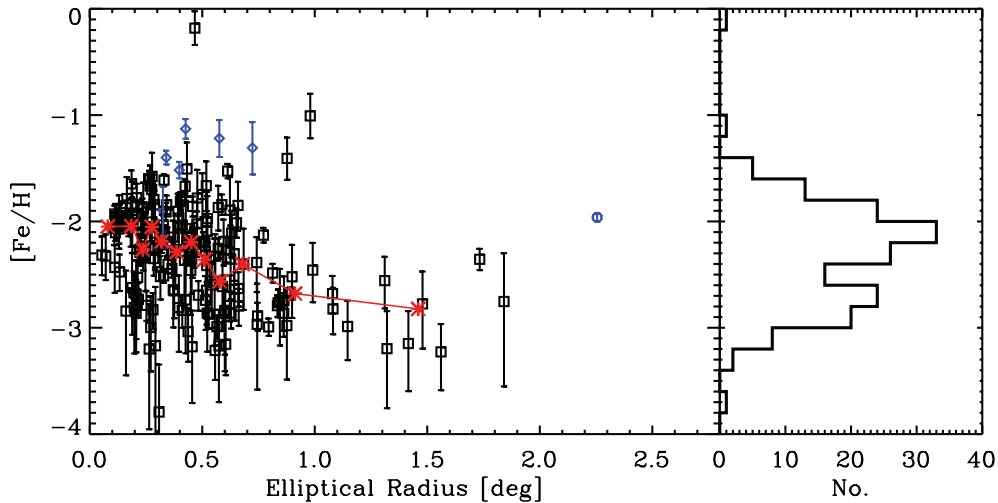


Figure 8. Left: metallicity distribution as function of elliptical radius for the probable members of Sextans (squares with error bars). The diamonds with error bars show those stars whose velocities fall within the 3σ range of membership, but that are likely non-members based on their large Mg I EW ($>0.5 \text{ \AA}$). The small blue circle indicates the star with peculiar location on the CMD. Since the stars represented with the diamonds and the blue circle are likely non-members they will not be considered when deriving properties relative to Sextans. The red asterisks connected by a solid line represent a running median over 15 stars (except for the last point, which is over nine stars). Right: metallicity distribution for Sextans members (from the squares in right-hand side panel).

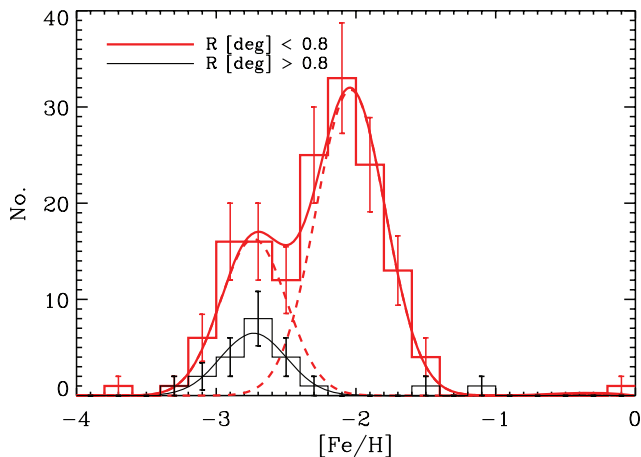


Figure 9. Metallicity distribution for Sextans probable members at projected radii $R < 0.8$ (thick red histogram) and at $R > 0.8$ (thin black histogram). The solid black thin line shows the Gaussian fit to the distribution at $R > 0.8$; the thick solid red line shows the best fit to the distribution at $R < 0.8$ for a sum of two Gaussians; the position of the central $[\text{Fe}/\text{H}]$ and dispersion of one of the two Gaussian is kept constant to the values found for the distribution at $R > 0.8$. The dashed lines show the two Gaussians separately. The error bars are Poissonian.

‘metal-rich’ component is that of the ‘metal-poor’ stars.² We will come back to this point in Section 4.3.2.

Fig. 9 also shows the presence of 31 stars with CaT $[\text{Fe}/\text{H}] < -2.8$, whose presence was not revealed when using the CaT calibration based on globular clusters; 11 of these stars have $[\text{Fe}/\text{H}] < -3$, i.e. they could be classified as extremely metal poor stars. The

² Here the Gaussian fit to the metallicity distribution at different distances from the centre is only meant to highlight the differences in the peak metallicity value between the inner and outer parts.

presence of stars of these metallicities excludes the hypothesis that Sextans was formed from a pre-enriched medium of $[\text{Fe}/\text{H}] > -3$ as Helmi et al. (2006) put forward.

Seven Sextans stars with CaT $[\text{Fe}/\text{H}] \lesssim -2.7$ have been followed up at high spectral resolution by Aoki et al. (2009) and Tafelmeyer et al. (2010), showing that the CaT calibration holds down to these low metallicities.

4.2 Velocity gradients

Early studies on dSphs, based on data sets of dozens of line-of-sight velocities in the central regions of these objects, had not yielded statistically significant detections of velocity gradients in these galaxies and therefore dSphs have commonly been regarded as exclusively pressure-supported systems. The gathering of much larger data sets, with hundreds line-of-sight velocities spread throughout the face of dSphs, led to the detection of velocity gradients in several of these objects.

Fig. 10 shows a velocity field for Sextans obtained from the probable members of the galaxy. There are hints of the presence of a velocity gradient along the projected major axis of Sextans, but from this plot it is also evident that, given the small number of stars distributed over a large area, more details, such as velocity contours, cannot be reliably obtained.

We analyse the velocity trends of the probable members along different directions across the face of the galaxy. Given the relatively sparse spatial sampling, we explore only four directions: along the major and minor axes [position angle (PA) = 56° , 146° , respectively] and along two intermediate axes (PA = 101° , 191°). We consider a slit of variable width along those axes and explore the trend of the line-of-sight velocity in the GSR frame as a function of the linear distance from the centre of the galaxy for those stars within the ‘slit’. We decided not to bin the data, as they are too sparse.

Fig. 11 shows the results for a slit width of 0.3 . As fiducial functional form for the gradient we use a straight line, with the intercept

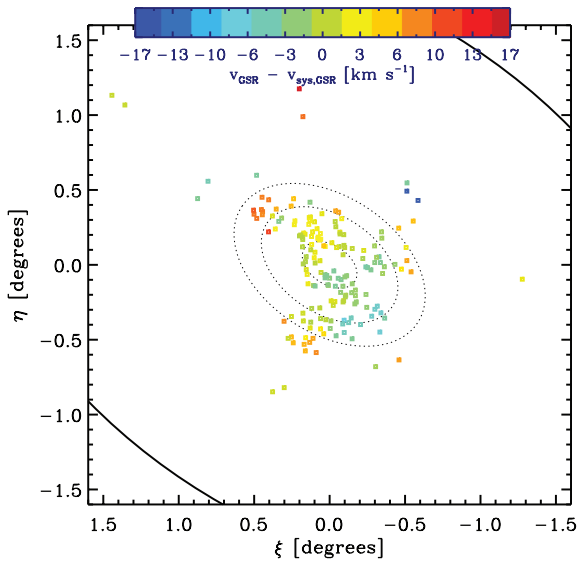


Figure 10. Velocity field for probable members to Sextans. The velocities are smoothed with a ‘median filter’, i.e. we associate to each star the median velocity of the stars located within a square of side 0.2 centred on the considered star; this smoothing is just for visual purposes and aims at reducing the velocity variations due to the dispersion of the galaxy. We use the velocities in the GSR frame to avoid spurious gradients introduced by the component of the Sun and LSR motions along the line of sight to Sextans. The colour bar gives the velocity scale. The dotted ellipses are placed at 0.2, 0.5 and 0.7 to give an idea of the distance scale. The solid ellipse shows the nominal tidal radius (from Irwin & Hatzidimitriou 1995).

fixed to the systemic velocity, and we perform an unweighed fit to the data points referring to the probable members. In order to derive the error in the fitted slope, we create 10 000 mock velocity data sets in which the stars are as many as the number of probable members and with the same positions, but the velocities are drawn from Gaussians centred on the measured velocities and with dispersion given by the velocity errors and the global dispersion of Sextans added in quadrature. For each of these mock data sets we repeat the unweighed fit to the velocities along the various axes; the error in the slope is given by the 1σ level in the distribution of fitted slopes. For this slit width the detected slopes are $8.5 \pm 3.0 \text{ km s}^{-1} \text{ deg}^{-1}$ along the major axis, $-0.8 \pm 4.2 \text{ km s}^{-1} \text{ deg}^{-1}$ along the minor axis, $0.4 \pm 5.3 \text{ km s}^{-1} \text{ deg}^{-1}$ along the axis at $\text{PA} = 101^\circ$ and $7.5^{+3.4}_{-3.0} \text{ km s}^{-1} \text{ deg}^{-1}$ along the axis at $\text{PA} = 191^\circ$.

In order to assess the significance of such detections we repeat the above procedure reshuffling the measured velocities 10 000 times, where this should be equivalent to eliminating any coherent motion and therefore simulating a non-rotating dSph with the same overall dispersion as measured for Sextans. We then calculate how many times the mock data sets give amplitudes larger than the measured ones. For a slit width of 0.3 the percentages are 0.4, 58.4, 46.9 and 0.9 per cent along the major, minor, $\text{PA} = 101^\circ$ and $\text{PA} = 191^\circ$ axes, respectively.³ The only statistically significant detections appear to be the ones along the major axis and along the axis at $\text{PA} = 191^\circ$. If these velocity gradients are due to rotation about the minor axis of

³ We checked whether the gradient along the $\text{PA} = 191^\circ$ axis may be driven by the two points at distance larger than 0.9, by repeating the determination removing these two points. The gradient is still present, $6.3 \pm 3.7 \text{ km s}^{-1} \text{ deg}^{-1}$, although the significance slightly decreases (the percentage of mock data set giving as large a gradient increases to 4.5 per cent).

Sextans, we would expect to detect similar velocity gradients along the $\text{PA} = 101^\circ$ and 191° axes, given that they are symmetric about the minor axis; however, while the spatial coverage along the $\text{PA} = 191^\circ$ is quite homogeneous and symmetric about the centre of the galaxy, this is not the case along the $\text{PA} = 101^\circ$ axis, along which we have data only in the north-west part of the galaxy; it is therefore unclear if the discrepancy in the detection is due to the difference in spatial coverage.

We find that, when increasing the slit width, for example to 0.4, the amplitude of the gradients slightly decreases, which suggests that the kinematics along a certain axis starts to be contaminated by the inclusion of more stars moving differently because placed at different distances from the centre. In this case the percentage of the mock data sets giving amplitudes larger than the measured ones is larger than for a slit width of 0.3, but the gradients along the projected major axis and the $\text{PA} = 191^\circ$ axis remain statistically significant.

Another concern in the derivation of the velocity gradient is the possible inclusion in the sample of contaminants from the MW, or vice versa the possible exclusion of Sextans stars based on the 3σ cut-off. However, none of the two points appears to be an issue in the analysis here carried out as it is visible from Fig. 11 where we also show the non-members falling in the considered slits: from these figures it is clear that the fraction of unidentified contaminants still present in the 3σ velocity range is likely to be negligible, and also that we are unlikely to have missed probable members because of the 3σ cut-off.

As mentioned already, with the current spatial sampling it is difficult to extract a velocity field and to determine a rotation pattern. We adopt a simple empirical approach and assume that $v_{\text{rot}} = k d_{\text{min}}$, where $k = 8.5 \text{ km s}^{-1} \text{ deg}^{-1}$ and d_{min} is the angular distance of each star from the minor axis along a direction parallel to the major axis (with d_{min} positive above the minor axis and negative below the minor axis, the formula gives receding and approaching velocities above and below the minor axis, respectively). To assess how good a representation of the data this is, we subtract the v_{rot} from the stars classified as probable members, and re-derive the velocity field and the trends along the various slits. There appears to be a residual pattern in the velocity field from the ‘rotation-subtracted’ velocities; indeed, velocity gradients are still present along the various axes, but they do not appear to be statistically significant. For a slit width of 0.3 the detected slopes are $-0.1 \pm 3.1 \text{ km s}^{-1} \text{ deg}^{-1}$ along the major axis, $-1.8^{+4.5}_{-3.9} \text{ km s}^{-1} \text{ deg}^{-1}$ along the minor axis, $7.1^{+5.2}_{-5.5} \text{ km s}^{-1} \text{ deg}^{-1}$ along the axis at $\text{PA} = 101^\circ$ and $1.6 \pm 3.1 \text{ km s}^{-1} \text{ deg}^{-1}$ along the axis at $\text{PA} = 191^\circ$. The percentages of mock data sets that give amplitudes larger than the measured ones are large, 48.4, 66.4, 9.0 and 30.6 per cent along the major, minor, $\text{PA} = 101^\circ$ and $\text{PA} = 191^\circ$ axes, respectively, i.e. the gradients do not appear to be highly statistically significant, meaning that the rotation pattern we assume is a reasonable representation of the data.

It appears that a weak velocity gradient is present in Sextans, but the direction and amplitude of this gradient is difficult to constrain. Note that our determination differs from the determination by Walker et al. (2008), who find a gradient of $-2.1 \pm 0.8 \text{ km s}^{-1} \text{ deg}^{-1}$ along a $\text{PA} = 120^\circ$. Given that the velocities between the two studies compare well (see the appendix), this difference is most likely due to the different coverage and size of the sample, as well as the methodology used. A larger statistical sample and coverage of the galaxy would help quantifying this better; however, given the low surface brightness and large extent on the sky of Sextans, this may be a challenging task.

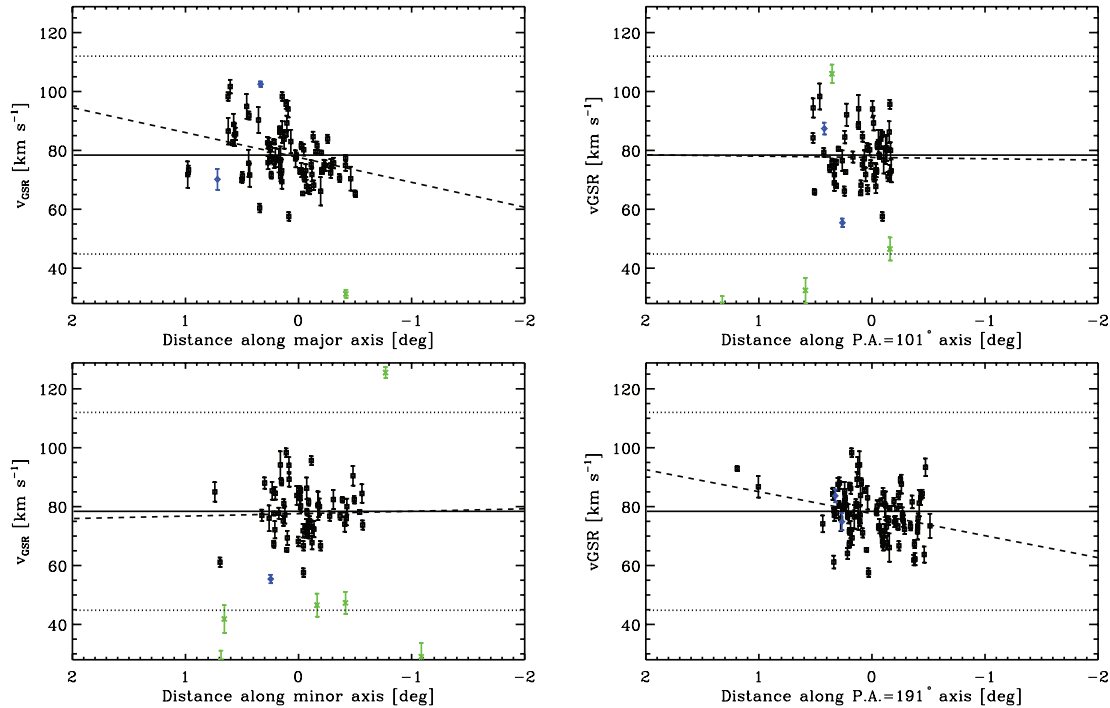


Figure 11. v_{GSR} for probable Sextans members versus distance along axes at PA = 56° (major axis), 101° , 146° (minor axis), 191° for stars located within ± 0.15 from these axes (squares with error bars). The probable non-members within the same spatial region are shown as diamonds and crosses with error bars (stars with velocity consistent with membership but with Mg I EW too large for giant stars and stars with velocity outside the 3σ selection region, respectively). The solid line indicates the systemic velocity of Sextans; the dotted lines indicate a region in velocity of $\pm 5\sigma$ from the systemic; the dashed line shows the best-fitting straight line to the data (see the text for the values of the best fit).

4.3 Observed velocity dispersion profile

4.3.1 All members

We derive the line-of-sight velocity dispersion profiles for Sextans by binning the velocities of stars at similar radii using the sample of probable members as determined in Section 3.4 and deriving the average velocity and dispersion per bin using the procedure described in Hargreaves et al. (1994).

In deriving the line-of-sight velocity dispersion profile we checked for the effect of a number of issues.

First, we check the effect that the number of stars per bin has on the derived line-of-sight velocity dispersion profile by fixing the number of stars per bin to a constant value of $N = 20, 25, 30$ and 35 (except for the last bin, which is allowed to have a lower number of points). We find that, even though the shape and amplitude of the line-of-sight velocity dispersion profiles are consistent within the error bars among all the cases, the binning with $N = 35$ stars is the most reliable one because it produces less oscillations in the trend of average velocities per bin, and that these velocities are consistent with the systemic velocity.

We then explore the effect of binning the data in elliptical annuli of constant ellipticity and PA ($e = 0.35$ and PA = 56°), and circular annuli, using a constant number of $N = 35$ stars per bin. In fact, one uses stars with a non-spherical spatial distribution as kinematic tracers of an underlying distribution which may be spherical (as well as oblate, prolate or even triaxial). We also use a constant number of $N = 35$ stars per bin when exploring the effect of subtracting the detected velocity gradient on to the determination of the velocity dispersion profile (hereafter we refer to the profile derived from

the individual velocities from which the velocity gradient has been subtracted as the ‘rotation subtracted’ profile). These results are shown in Fig. 12 (left): the line-of-sight velocity dispersion profiles derived from the elliptical and circular binning, when subtracting or not rotation, all agree with each others within the error bars. In the following we adopt the rotation subtracted velocities and the elliptical binning.

The effect of using bins of variable width which increases with projected radius, instead than using a constant number of stars per bin, is shown in the right-hand panel of Fig. 12. We explored three different binnings, which are labelled as ‘Binning1’, ‘Binning2’ and ‘Binning3’ in the right-hand panel of Fig. 12. All these choices of binning are compatible with the trend shown when keeping the number of probable members per bin constant. In the following, when deriving the mass profile of Sextans we will use the line-of-sight velocity dispersion profile from ‘Binning2’; however, the effects of a different binning on the mass determination will also be considered, by checking the results obtained when using the profile from ‘Binning3’. We will not use ‘Binning1’ for the analysis because it represents the case where the average velocity per bin differs the most from the systemic.

The line-of-sight velocity dispersion profile of Sextans appears to slightly increase with radius although, given the large size of the error bars in the last bins, it is also compatible with remaining constant.

To compare the line-of-sight velocity dispersion profile published by Walker et al. (2007) and ours we should consider the case of the circular binning, with no velocity gradient subtracted: in this case our profile remains approximately constant around 8 km s^{-1} , consistent with the determination by Walker et al. (2007).

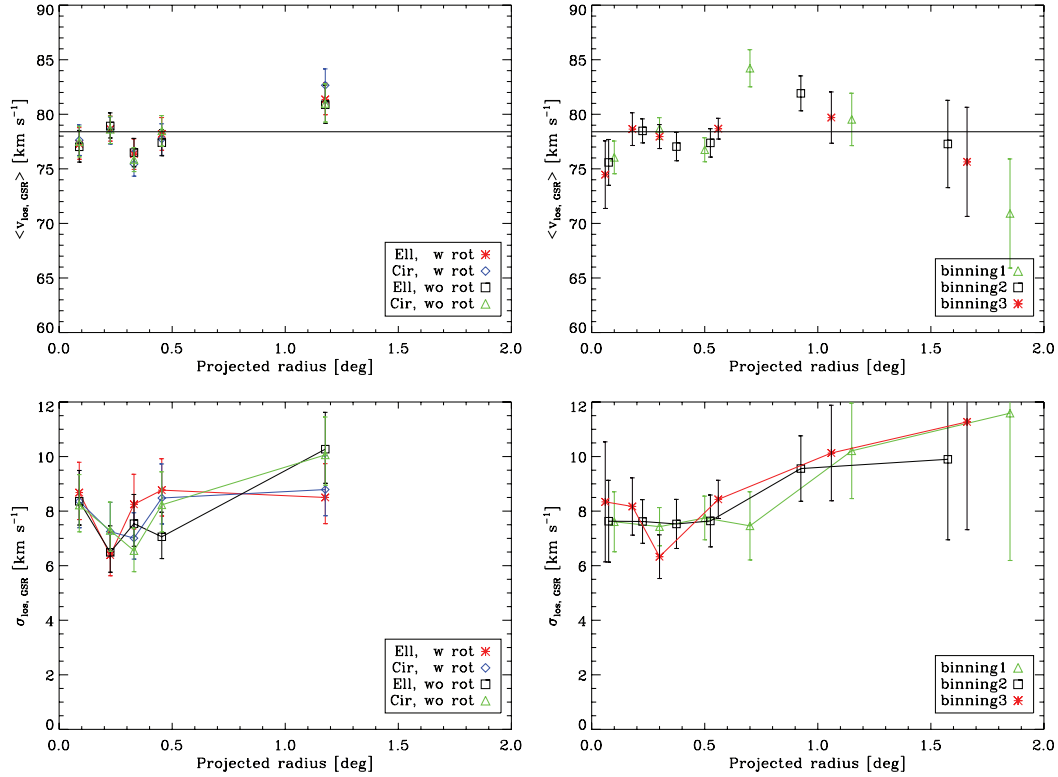


Figure 12. Line-of-sight average velocity (top) and velocity dispersion profile (bottom) in GSR system for probable Sextans members versus projected radius. Left: profiles derived keeping the number of stars per bin approximately constant to 35 stars per bin; the profiles have been derived both when the velocity gradient is included (asterisks: elliptical binning; diamonds: circular binning) and when it is subtracted from the individual velocities (squares: elliptical binning; triangles: circular binning). Right: profiles derived for three different choices of binning with bins of increasing width with projected radius, in the case when the gradient is subtracted from the individual velocities and elliptical binning. The horizontal solid line in the top panel indicates the systemic velocity of Sextans.

4.3.2 ‘Metal-rich’ and ‘metal-poor’ stars

In previous work, we have combined the information on the spatial location, metallicity and velocity of individual stars in dSphs. This allowed us to explore links between the metallicity and the kinematics of stars in the Sculptor and Fornax dSphs (T04 and B06, respectively), and shown that in these systems metal-rich stars – centrally concentrated – have a smaller velocity dispersion than metal-poor stars – which in turn have a more extended spatial distribution. The metallicity chosen to illustrate this different kinematic behaviour between the colder and hotter stellar components is somewhat subjective, but it is chosen on the basis of considerations on the metallicity distribution in order to minimize contamination between the two metallicity components.

As seen in Section 4.1 at $R < 0.8$, the region where the whole range of metallicities is present, the metallicity distribution of Sextans is well approximated with the sum of two Gaussians, a ‘metal-rich’ and a ‘metal-poor’ one, which cross at $[\text{Fe}/\text{H}] \sim -2.3$. Therefore to minimize contamination between these two components, we exclude the range $-2.4 < [\text{Fe}/\text{H}] < -2.2$ and we derive the trend of mean velocity and dispersion for the stars more metal rich than $[\text{Fe}/\text{H}] = -2.2$ and more metal poor than $[\text{Fe}/\text{H}] = -2.4$ over different spatial bins.

Fig. 13 shows that also in Sextans ‘metal-rich’ and ‘metal-poor’ stars display a different behaviour (akin to our findings in the Fornax and Sculptor dSphs), with the former population in general kinematically colder than the latter. The profile of the metal-rich stars appears to be slightly declining, while for the metal-poor stars it is

everywhere constant (except in the first bin, see next section) and extends further than the profile for the metal-rich stars, as a consequence of the larger spatial extent of the metal-poor stars. It remains to be proven if the different spatial extent of the stellar population analysed is the only factor that causes the different kinematics, or if one needs to take into account also different orbital properties for the different stellar populations. Furthermore, the outer bin for the ‘metal-rich’ stars suffers from low number statistics and would certainly benefit from a larger sample of stars with $[\text{Fe}/\text{H}] > -2.2$.

4.4 Substructures

Kleyna et al. (2004) detected a kinematically cold substructure, with dispersion close to zero, from seven stars with radial velocity measurements in the inner 5 arcmin of Sextans. One of the hypotheses that they put forward is that the stars giving raise to this kinematic feature may belong to the remnant of a disrupted stellar cluster which spiralled into Sextans centre. The authors note that this hypothesis can account for the sharp central rise in the light distribution of Sextans (e.g. Irwin & Hatzidimitriou 1995). Also the distribution of blue stragglers in Sextans, with the brighter (i.e. more massive) blue stragglers more centrally concentrated than the fainter ones (Lee et al. 2003) could be explained by this mechanism. The authors estimate a luminosity of $1.3 \times 10^5 L_{\odot}$ for the disrupted cluster. The existence of this central cold substructure has not been confirmed by subsequent studies such as Walker et al. (2006), who instead find another cold substructure of estimated

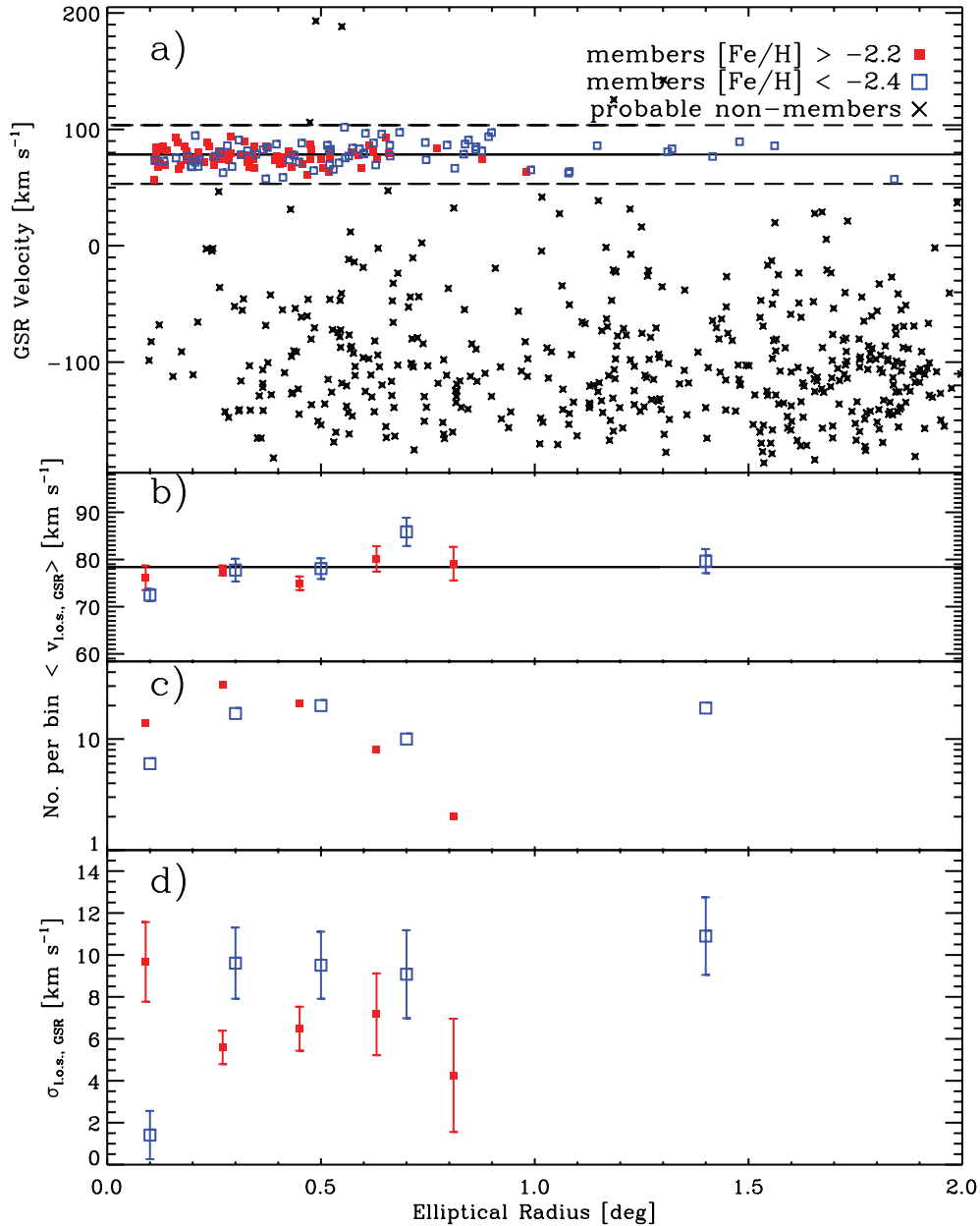


Figure 13. Kinematic properties for probable Sextans members more metal rich than $[\text{Fe}/\text{H}] = -2.2$ (red filled squares) and more metal poor than $[\text{Fe}/\text{H}] = -2.4$ (blue open squares). We show the variation of the rotation-subtracted GSR velocity versus elliptical radius (a); average rotation-subtracted GSR velocity (b); number of stars (c); velocity dispersion profile using rotation-subtracted GSR velocities (d). The solid horizontal line indicates the systemic velocity, the horizontal long-dashed lines show the region used for the 3σ membership selection.

luminosity $\sim 10^4 L_{\odot}$ at a different location, i.e. around the core radius of the galaxy.

The inner point in Fig. 13 shows peculiar characteristics for the metal-poor (MP) stars: the velocity dispersion is very cold, $1.4 \pm 1.2 \text{ km s}^{-1}$, and the average velocity is $72.5 \pm 1.3 \text{ km s}^{-1}$, about 4σ away from the systemic.⁴ In the binning used these values are derived from the six innermost metal-poor stars, however, from panel (a) of Fig. 13 it can be seen that other three MP stars at $R < 0:22$ share very similar velocities to this group of stars; only one

MP star at $R < 0:22$ is found at very different velocities and can therefore be thought of as belonging to the main Sextans population. This group of nine stars do not only share very similar distances and kinematics but also metallicities, with an average metallicity of $[\text{Fe}/\text{H}] = -2.6$ and a scatter of 0.15 dex. Note that the average metallicity error for the stars in the substructure is 0.29 dex, much larger than the measured scatter in the metallicity, which means that the intrinsic scatter is going to be much lower than 0.15 dex. The similar metallicity of the stars found in the cold kinematic substructure would point to these stars previously belonging to a single stellar population, i.e. a stellar cluster.

Note that the information on metallicity is useful for such kind of detections: when considering all the stars together in the inner bin,

⁴ Here with σ we denote the error in the determined average velocity for the substructure.

with no distinction made on metallicity, the velocity dispersion is much larger, consistent with the rest of the galaxy.

Assuming that the ratio of stars in the substructure (nine) with respect to the total number of probable Sextans members (174) is representative, then the substructure would account for 5 per cent of the overall Sextans population. Assuming a luminosity for Sextans from Table 1 and a stellar mass-to-light ratio $(M/L)_{\text{lum},V} = 2$ typical of globular clusters (Illingworth 1976; Pryor et al. 1988) as plausible for an old stellar population, then crude estimates of the total luminosity and mass of this structure are $2.2 \times 10^4 L_{\odot}$ and $4.4 \times 10^4 M_{\odot}$. If this substructure is the same one found in Kleyna et al. (2004), our estimated luminosity is approximately one order of magnitude smaller than what Kleyna et al. (2004) estimated, i.e. $1.3 \times 10^5 L_{\odot}$. However, the estimate was carried out in a different way, where Kleyna et al. (2004) assumed that all the light in the central 10 arcmin is due to cluster debris.

We can instead assume that the estimated light in the central 10 arcmin, $1.3 \times 10^5 L_{\odot}$, is actually given by the sum of the light from the substructure plus the light from the overall Sextans population. We then use the value of the central surface brightness from Irwin & Hatzidimitriou (1995) – derived excluding the central point giving rise to the sharp central rise in the light distribution of Sextans – to estimate the contribution of the overall Sextans population to the light in the central 10 arcmin: this is about $7.8 \times 10^4 L_{\odot}$. Therefore the contribution of the substructure would then amount to $5.2 \times 10^4 L_{\odot}$, much closer to our estimate. It is therefore possible that the substructure here detected is the same one as in the work of Kleyna et al. (2004).

The properties we find are compatible with other cold substructures found in other dSphs, such as in Ursa Minor by Kleyna et al. (2003), in Sculptor (Battaglia 2007) and at projected distances of about 1 core radius in Sextans (Walker et al. 2006). This luminosity corresponds to an absolute $M_V = -6.2$, which is similar to globular clusters found in the Fornax, Sagittarius dSphs and in other dwarf galaxies (e.g. see van den Bergh 2006).

To date, the most metal poor known globular cluster resides in the Fornax dSph, with high resolution measurements yielding a $[\text{Fe}/\text{H}] = -2.5$ (Letarte et al. 2006). If the stars in the cold substructure here detected do indeed belong to the remnant of a disrupted globular cluster, the $[\text{Fe}/\text{H}]$ values we measure would place it among the most metal poor globular clusters known. Given the large error bars of the individual CaT measurements for these stars, determinations from high-resolution spectroscopic measurements would be needed to place this on a secure foot. Detection of the O–Na anticorrelation would confirm the hypothesis.

Note that the CaT $[\text{Fe}/\text{H}]$ values are calculated assuming that the stars in the substructure are at the same distance of Sextans. If those stars are actually an external feature, then the $[\text{Fe}/\text{H}]$ values would not be correct. However, given the average velocity of the substructure well within $1\sigma_{\text{GSR}}$ from the systemic velocity of Sextans, it is likely that these stars do indeed belong to the dSph.

5 MASS DETERMINATION

We determine the mass of Sextans by means of Jeans modelling of a spherical and stationary system assuming different DM density profiles.

The methodology we use consists of comparing the observed line-of-sight velocity dispersion σ_{los} for each distance bin with that predicted from the Jeans modelling for different models of the DM density profile and hypothesis on the velocity anisotropy of the

tracer⁵ (see Section 5.1). We explore the space of parameters which define each model and determine the χ^2 as

$$\chi^2 = \sum_{i=1}^{N_{\text{bins}}} \left(\frac{\sigma_{\text{los}i} - \sigma_{\text{los}}(R_i; p_{\beta}, p)}{\epsilon_i} \right)^2. \quad (2)$$

The variable p denotes a characteristic mass parameter of each DM model, p_{β} denotes a parameter describing the behaviour of the velocity anisotropy (see Section 5.2). Finally, ϵ_i is the error in the observed line-of-sight velocity dispersion. The best-fitting parameters are defined as those for which χ^2 is minimized. We quote as errors in the individual parameters the projections of the $\Delta\chi^2 = 2.3$ region (corresponding to the region of 68.3 per cent *joint* probability for a two free parameters χ^2 distribution).

5.1 Predicted velocity dispersion profile

The Jeans equation for a stationary spherical system in absence of net streaming motions in any of the directions is (Binney & Tremaine 1987)

$$\frac{1}{\rho_*} \frac{d(\rho_* \sigma_{r,*}^2)}{dr} + \frac{2\beta \sigma_{r,*}^2}{r} = -\frac{d\phi}{dr} = -\frac{V_c^2}{r}, \quad (3)$$

where ρ_* is the density of the tracer; β is the velocity anisotropy parameter, defined as $\beta = 1 - \sigma_{\theta,*}^2/\sigma_{r,*}^2$, assuming $\sigma_{\theta,*}^2 = \sigma_{\phi,*}^2$; $\sigma_{r,*}$, $\sigma_{\theta,*}$ and $\sigma_{\phi,*}$ are the velocity dispersions in the (r, θ, φ) direction, respectively; ϕ and V_c are the potential and the circular velocity of the total mass distribution. Note that $\beta = 0$ if the velocity ellipsoid is isotropic, $\beta = 1$ if the ellipsoid is completely aligned with the radial direction, and $\beta < 0$ for tangentially anisotropic ellipsoids.

The quantity to compare to the observations is the line-of-sight velocity dispersion of the tracer population (Binney & Mamon 1982):

$$\sigma_{\text{los}}^2(R) = \frac{2}{\Sigma_*(R)} \int_R^{\infty} \frac{\rho_*(r) \sigma_{r,*}^2 r}{\sqrt{r^2 - R^2}} \left(1 - \beta \frac{R^2}{r^2} \right) dr, \quad (4)$$

where R is the projected radius (on the sky) and $\Sigma_*(R)$ is the mass surface density of the tracer.

We refer to Mamon & Łokas (2005) for the derivation of the line-of-sight velocity dispersion profile from the Jeans equation using different hypotheses on β .

As the discovery of multiple stellar populations in dSphs is a recent one, traditionally dSph galaxies have been treated as single component systems. In Battaglia et al. (2008b) we modelled each stellar component separately in the Sculptor dSph, showing that this allows to relieve some of the degeneracies. This kind of analysis needs imaging such that the surface number density profiles of the different components can be accurately determined. This is not the case to date for Sextans, therefore until better photometric data will come we will treat all the stars in Sextans as in one component.

Below we discuss in detail the ingredients to solve the Jeans equation.

(i) *The spatial distribution of the tracer:* Irwin & Hatzidimitriou (1995) found that the surface brightness profile of Sextans is best fit by an exponential profile with scale radius $R_e = 15.5$ arcmin. This is equivalent to assuming a Sersic profile with Sersic radius $R_S = 15.5$ arcmin and shape parameters $m = 1$ as done by Walker

⁵ By ‘tracer population’ we mean those objects whose kinematics can be used to recover properties of the total potential. In this case our tracers are the spectroscopically observed RGB stars.

et al. (2007) and Łokas (2009). For the mass-to-light ratio we use $(M/L)_V = 1 (M/L)_{V,\odot}$ and luminosity and distance from Table 1. The three-dimensional (3D) density profile is derived from the surface brightness profile through inversion of Abel integrals, assuming that the stars are spherically distributed. We refer to Łokas, Mamon & Prada (2005) for all the relevant formulas.

(ii) *The kinematics of the tracer – velocity gradient*: the expression for the projected velocity dispersion (equation 4), which measures the projected random motion in a galaxy, has been derived for the hypothesis that the system is not rotating. In systems where the rotation law can be accurately derived and there is enough statistics to derive the dispersion profile along both the major and minor axes, one can use the Jeans equations in cylindrical coordinates. The present coverage of this data set does not allow this alternative. Therefore we use the observed line-of-sight velocity dispersion profile derived from the rotation subtracted individual velocities.

(iii) *The kinematics of the tracer – velocity anisotropy*: since the variation of the velocity anisotropy with radius is not known (as this requires proper motions), we consider two hypotheses: β constant with radius; and using the Osipkov–Merritt parametrization for β (Osipkov 1979; Merritt 1985):

$$\beta_{\text{OM}} = r^2 / (r^2 + r_a^2), \quad (5)$$

where r_a is the anisotropy radius. In the Osipkov–Merritt parametrization the anisotropy is always ≥ 0 , i.e. it is never tangential. The central regions are isotropic, and for $r_a \rightarrow \infty$ the anisotropy becomes purely radial. At $r = r_a$, $\beta = 0.5$. The smaller r_a , the faster the anisotropy becomes very radial. Models with large r_a correspond to models with almost isotropic behaviour.

(iv) *Total mass distribution*: since from previous works the contribution of the stars to the overall potential has been shown to be negligible in Sextans and in dSphs in general, we consider the DM halo as the only contributor to the kinematics of the tracer population.

We consider two different models for a spherically symmetric DM halo potential.

Pseudo-isothermal sphere: this model has been extensively used in the context of extragalactic rotation curve work (see Swaters, Madore & Trewheella 2000, and references therein). The density profile associated to this model is

$$\rho(r) = \rho_0 \frac{r_c^2}{(r_c^2 + r^2)}, \quad (6)$$

where r_c is the core radius, $\rho_0 = [V_c^2(\infty)/4\pi G r_c^2]$ is the central density and $V_c(\infty)$ is the asymptotic circular velocity. At large radii the density behaves as $\rho \propto r^{-2}$.

The resulting mass profile is

$$M(< r) = 4\pi\rho_0 r_c^2 \left(r - r_c \arctan \frac{r}{r_c} \right). \quad (7)$$

The profile is completely defined by ρ_0 and r_c , or any couple of non-degenerate parameters.

NFW model: this profile is motivated by cosmological N -body simulations in a CDM framework (Navarro, Frenk & White 1996, 1997). In this case the DM density profile is given by

$$\rho(r) = \frac{\delta_c \rho_c^0}{(r/r_s)(1 + r/r_s)^2}, \quad (8)$$

where r_s is a scale radius, ρ_c^0 the present critical density and δ_c a characteristic overdensity. The latter is defined by $\delta_c = [100 c^3 g(c)]/3$, where $c = r_v/r_s$ is the concentration parameter of the halo, r_v its

virial radius, and $g(c) = (\ln(1+c) - c/(1+c))^{-1}$. The concentration c has been found to correlate with the halo virial mass M_v in the range $10^{11} - 10^{14} h^{-1} M_\odot$ (Navarro et al. 1997; Bullock et al. 2001; Wechsler et al. 2002), so that at a given redshift more massive haloes have lower concentrations. In principle, the relation between c and M_v makes the NFW model completely defined by one parameter (e.g. M_v). However at a fixed mass the scatter in the predicted concentration is large, of the order of $\Delta(\log_{10} c) = 0.18$ (Bullock et al. 2001), thus we do not consider the NFW density profile as a one-parameter family, but we describe it both by the concentration c and by the virial mass or the circular velocity at the virial radius.

At large radii (for $r \gg r_s$), the density behaves as $\rho \propto r^{-3}$, and therefore, the total mass diverges logarithmically. The resulting mass profile is

$$M(< r) = M_v \frac{f(x)}{f(c)}, \quad (9)$$

where $x = r/r_s$ and $f(x) = \ln(1+x) - [x/(1+x)]$ (Klypin, Zhao & Somerville 2002).

When integrating equation (4), we set the upper integration limit to r_v where we use $r^{2\beta} \rho_* \sigma_{r,*}^2 |_{r_v} = 0$ (we are essentially assuming that the particles are bound out to the virial radius). As we will see in the next section and as it is found in previous works on dSphs, the extent of the luminous matter is typically one order of magnitude smaller than the extent of the best-fitting DM halo, thus setting the upper integration limit to r_v instead of to infinity will not affect our results, only decrease the computation time.

5.2 Results

We perform the fitting procedure for the observed line-of-sight profile derived in Section 4.3.1, i.e. ‘Binning2’.⁶ The parameter p in equation (2) denotes the mass enclosed within the last measured point for the isothermal sphere and the virial mass for the NFW model; the parameter p_β is $p_\beta = \beta$ for the models using β constant with radius and $p_\beta = r_a$ for the models using β_{OM} .

The results are summarized in Table 4.

(i) *Isothermal sphere*: in this model the total mass of the DM halo is not finite, therefore, we choose to fit the value of the mass within the last measured point, $M(< R_{\text{last}})$, which for ‘Binning2’ is $R_{\text{last}} = 2.36$ kpc. The other free parameter to take into account is the velocity anisotropy β .

We explore the performance of models with core radii $r_c = 0.001, 0.05, 0.1, 0.5, 1, 1.5, 2, 2.5$ and 3 kpc. In practise, we fix the core radius to each of these values and minimize the χ^2 to obtain the best-fitting $M(< R_{\text{last}})$ and β . The results of the fits are summarized in the plots shown in Fig. 14 (left). At a given core radius, the best-fitting models with constant β give in general smaller χ^2 values than when $\beta = \beta_{\text{OM}}$. The models for $\beta = \beta_{\text{OM}}$ and $r_c < 0.5$ kpc have a reduced $\chi^2 > 3$, which for 4 degrees of freedom corresponds to a significance level of less than 2 per cent; they can therefore be considered as statistically unacceptable. All the other best-fitting models for the explored core radii have reduced $\chi^2 \lesssim 1$, therefore, they are all statistically acceptable. For these models the best-fitting $M(< R_{\text{last}})$ ranges from ~ 1 to $4 \times 10^8 M_\odot$ (smaller core radii,

⁶ We checked that using the ‘Binning3’ velocity dispersion profiles produces best-fitting parameters and models that are very similar to those obtained when adopting the ‘Binning2’ profile, although in this case the minimum χ^2 values for the best-fitting models are larger than the ones from ‘Binning2’.

Table 4. Parameters of the best-fitting DM models for mass modelling of Sextans, when using the observed line-of-sight velocity dispersion profile from ‘Binning2’. The columns show the χ^2 , the reduced χ^2 (with the number of degrees of freedom being $\nu = 4$), the parameter defining the anisotropy (i.e. β itself for the $\beta = \text{const}$ case, and the anisotropy radius r_a (kpc) for the $\beta = \beta_{\text{OM}}$ case), the mass contained within the last measured point (at ~ 2.3 kpc, assuming a distance to Sextans of 86 kpc) and for the cuspy profile the virial mass.

	χ^2	χ^2/ν	p_β	$M(<R_{\text{last}})$	M_ν
Cored $r_c = 3.0$ kpc $\beta = \text{const}$	0.73	0.2	$0.06 < \beta < 0.6$	$4.0 \pm 0.7 \times 10^8 M_\odot$	
Cored $r_c = 1.5$ kpc $\beta = \beta_{\text{OM}}$	2.5	0.6	$r_a > 1.5$ kpc	$3.2 \pm 0.7 \times 10^8 M_\odot$	
Cuspy $c = 10$ $\beta = \text{const}$	2.9	0.7	$-1.4 < \beta < 0$	$1.9 \pm 0.6 \times 10^8 M_\odot$	$2.6 \pm 0.8 \times 10^9 M_\odot$

smaller masses); the best-fitting anisotropies ranges from -6 to 0.5 for $\beta = \text{const}$ (smaller core radii more tangential anisotropies), while the anisotropy radius goes from 2 to 15 kpc (the upper limit of the explored r_a), forcing the anisotropy to be close to zero. The models with the smallest reduced χ^2 (see Fig. 15) for $\beta = \text{const}$ have $r_c = 3$ kpc [$M(<R_{\text{last}}) = 4 \pm 0.8 \times 10^8 M_\odot$ and $0.06 < \beta < 0.6$] and for $\beta = \beta_{\text{OM}}$, $r_c = 1.5$ kpc [$M(<R_{\text{last}}) = 3.2 \pm 0.7 \times 10^8 M_\odot$ and $r_a > 1.5$ kpc].

This tendency for increasing tangential anisotropy with decreasing core radius comes from the fact that smaller core radii models have higher concentrations of mass in the central regions and this tends to increase the central value of the velocity dispersion. To match a nearly constant velocity dispersion profile the anisotropy then needs to be tangential.

(ii) *NFW model*: for this model we let the concentration vary from $c = 10, 15, 20, 25, 30, 35$, and for each of these values we derive the best-fitting virial mass and velocity anisotropy. Using an extrapolation of the formulae in the N -body simulations of Jing (2000) (see Koch et al. 2007b), the concentrations adopted here would correspond to the concentrations expected for haloes with virial masses in the range 10^6 – $10^{12} M_\odot$ (smaller mass larger c) well containing the range of virial masses expected for dSphs.

At fixed concentration, all the models with $\beta = \beta_{\text{OM}}$ have reduced χ^2 larger than then models with $\beta = \text{const}$. The models with $c \geq 20$ have a reduced $\chi^2 > 2.5$, corresponding to a significance level of less than 5 per cent for 4 degrees of freedom and have therefore low statistical significance. The best result for the $\beta = \text{const}$ case is also given by the model with $c = 10$, with a virial mass $M_\nu = 2.6 \pm 0.8 \times 10^9 M_\odot$ and $\beta = -0.6_{-1.4}^{+0.6}$ (see Fig. 15). All the models with $\beta = \text{const}$ have reduced χ^2 between 1 and 1.5, where the virial masses range from approximately 3×10^8 to $2.6 \times 10^9 M_\odot$ (smaller c larger virial mass), which gives a mass within the last measured point of 1 – $2 \times 10^8 M_\odot$, and β goes from about -4.5 to -0.6 (smaller c less tangential β). This also explains why most of the models with $\beta = \beta_{\text{OM}}$ are not favoured for NFW profiles: in the hypothesis of $\beta = \text{const}$, which yields a good fit to the data, the best-fitting anisotropies are mildly tangential; since in the $\beta = \beta_{\text{OM}}$ the anisotropy is forced to be positive, than the resulting model cannot reproduce the data as well.

We conclude that because of the well-known mass–anisotropy degeneracy, it is not possible to firmly distinguish between a cored and a cuspy DM distribution, nor about different hypothesis of anisotropy, solely on the basis of the line-of-sight velocity dispersion profile. The only models that can be excluded among the explored ones because of their large χ^2 values are the NFW models with $\beta = \beta_{\text{OM}}$ and $c \geq 20$. However, the general trend is for the best-fitting models to have β close to isotropic, be it slightly tangential as for the NFW case or slightly radial as for the cored profile. Also, the tendency for cuspy profiles of low concentrations to produce better fits than for larger concentrations seems to suggest

that shallower profiles are preferred. Independently on the model, we find that the mass within the last measured point of Sextans, at 2.3 kpc, should be in the range 2 – $4 \times 10^8 M_\odot$. This would give a dynamical mass-to-light ratio between 460 and $920 (M/L)_{V,\odot}$.

The presence of the central substructure does not affect the mass estimate derived. Although the velocity dispersion for stars at the distance covered by the substructure, $7.6 \pm 1.1 \text{ km s}^{-1}$, is lower than if these stars had not been included, i.e. $8.6 \pm 1.4 \text{ km s}^{-1}$, these two values are consistent within the errors.

6 DISCUSSION

(i) *Metallicity properties*: the stars in Sextans show a wide [Fe/H] range, with the majority having [Fe/H] values between -3.2 and -1.4 , with an average [Fe/H] = -1.9 . Among the sample of probable members, 11 extremely metal poor stars are found, reaching down to [Fe/H] = -3.8 . If the stars in Sextans were formed from a pre-enriched medium, then the presence of stars with [Fe/H] as low as -3.8 suggests that this interstellar medium most likely had not been pre-enriched to a larger value.

Sextans exhibits a clear spatial variation of its metallicity properties: the region at projected radius $R < 0.8$ displays the whole range of metallicities, while at larger projected radii practically only stars more metal poor than [Fe/H] ~ -2.2 are present. Photometric studies of its stellar population show an age difference of at least 3 Gyr between the central and outer parts of Sextans, with the central parts containing stars between 10 and 14 Gyr old and the outer parts mostly 14 Gyr old stars. It appears then that the outer parts were formed very quickly, reaching a metallicity up to [Fe/H] ~ -2.2 , while the inner parts could continue their evolution for at least 3 Gyr more and enrich to [Fe/H] ~ -1.4 . One can speculate that the less prolonged star formation of the outer parts may have been caused either from external processes, which removed the gas from the external region, or to internal effects, which depleted the outer parts of gas. It is although possible that gas was still present in the outer regions for some time but simply that conditions for star formation were not met.

Similar, although less pronounced, spatial variations of metallicity properties have been detected in other dSphs, such as for example in Sculptor (Tolstoy et al. 2004), Fornax (Battaglia et al. 2006) and to a minor extent in Carina (Koch et al. 2006). There are hints that Leo I may exhibit such variations (Gullieuszik et al. 2009) although the current data are not sufficient to put this result on a firm ground. Using Strömgren photometry Faria et al. (2007) show the presence of a possible spatial variation in the metallicity properties of the Draco dSph. It is still unclear what is the driving process behind these metallicity variations. To disentangle environmental effects from internal evolution it is important to obtain observations of the stellar populations, kinematics and metallicity variations of isolated dwarf galaxies, outside the halo of large spirals.

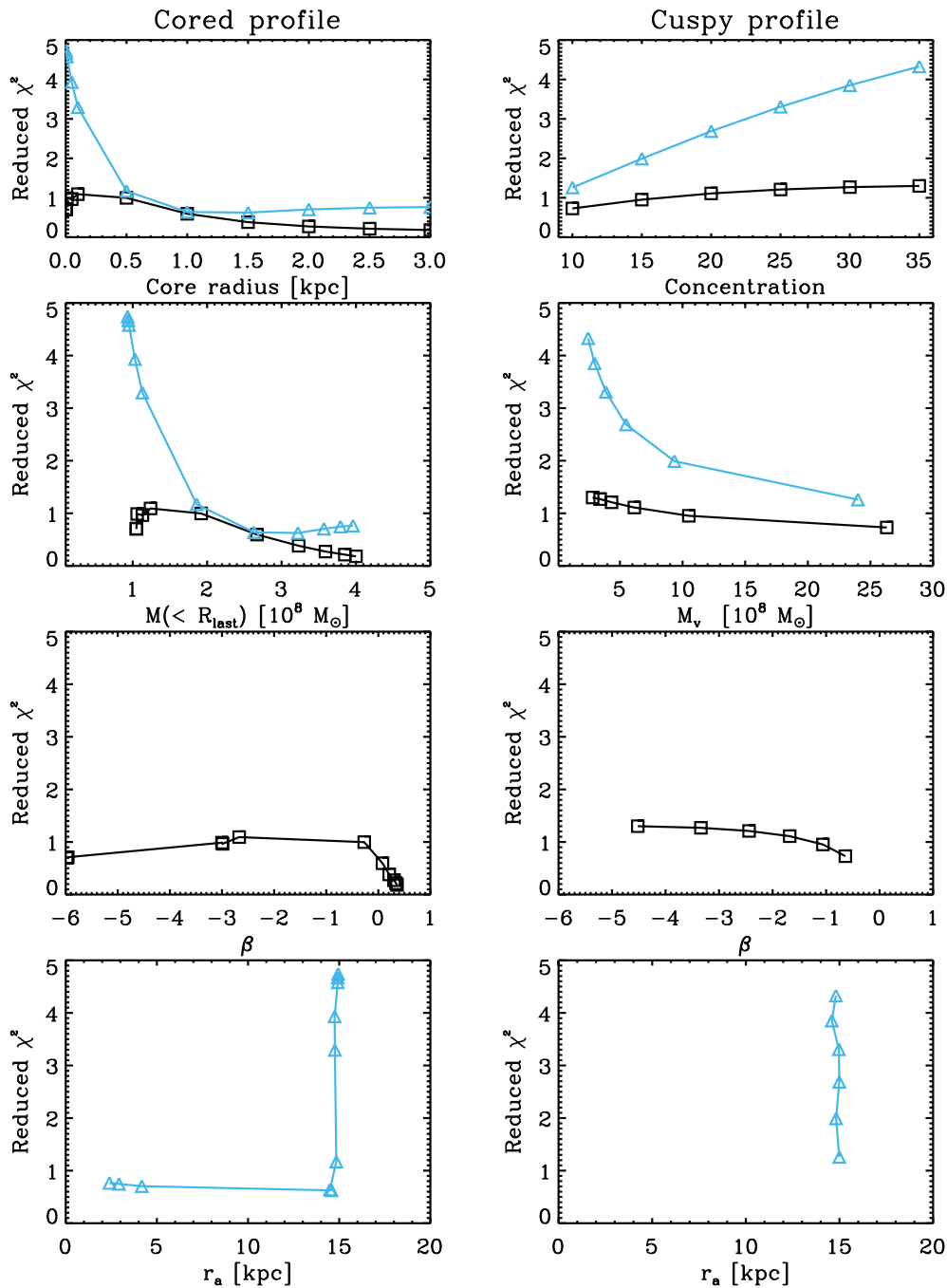


Figure 14. Here we summarize the results of the mass modelling when using the observed line-of-sight velocity dispersion profile derived with ‘Binning2’ (left: cored DM profile; right: cuspy DM profile). From top to bottom we plot the reduced χ^2 values for the best-fitting model as a function of core radius (left) and concentration (right), mass within the last measured point at ~ 2.3 kpc (left) and virial mass (right) both in units of $10^8 M_\odot$, velocity anisotropy in the hypothesis of constant anisotropy with radius, anisotropy radius in the hypothesis of velocity anisotropy following an Osipkov–Merritt profile. The black squares and cyan triangles show the results in the hypothesis of $\beta = \text{const}$ and $\beta = \beta_{\text{OM}}$, respectively. For each of the core radius (concentration) values shown in the top left (right) panel, the models are optimized over the anisotropy and mass parameters. The quoted reduced χ^2 values are therefore the value of the χ^2 for the best-fitting model over 4 degrees of freedom.

(ii) *Velocity gradient*: a statistically significant velocity gradient is found along the projected major axis and an axis at $\text{PA} = 191^\circ$ in our sample of 174 probable members of Sextans. Walker et al. (2008) also detect a velocity gradient in Sextans, although with lower amplitude and approximately along the minor axis of the galaxy. Pinning down the amplitude and direction of such gradients, expected to be small for dSphs, would require large sample of stars

not only in the central regions of the object but also in the outer parts, so that the trends along various directions may be accurately determined. Unfortunately this is very challenging for a system like Sextans, because of its large extent on the sky and the outer parts being sparsely populated.

Also a univocal interpretation of this feature does not appear possible at this stage. One possibility is that the gradient may have

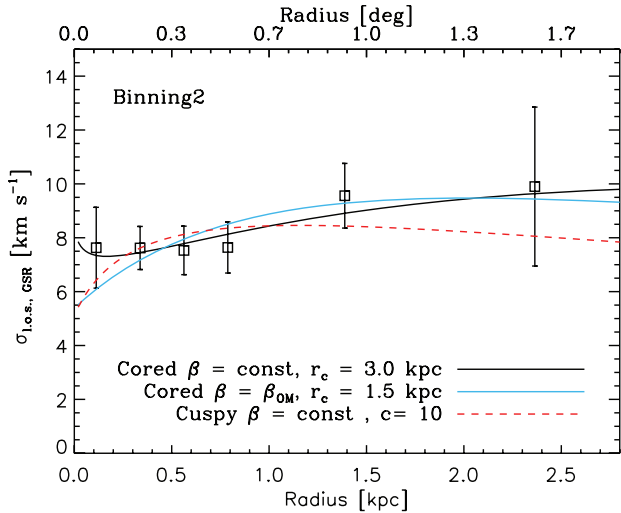


Figure 15. Observed line-of-sight velocity dispersion profile (squares with error bars) overlaid on the best-fitting model for a cored profile with β constant (solid black line), a cored profile with β_{OM} (solid cyan line), cuspy profile with β constant (dashed line) for ‘Binning2’.

originated as the result of tidal disruption of Sextans from the MW, as predicted in N -body models of disrupted satellites (e.g. Oh et al. 1995). However no clear signs of tidal disruption such as tidal tails or S-shaped contours are found in Sextans that could confirm this hypothesis, although this may be just due to the observational difficulties in detecting such features (e.g. Muñoz et al. 2008), especially in a diffuse and heavily contaminated object like Sextans. Knowledge of the accurate proper motion of the galaxy would allow to reconstruct its orbital history and determine if strong interactions with the MW may have occurred. However no direct determinations of the proper motion of Sextans are available yet in the literature. Such determinations would also allow to understand whether the observed gradient may merely be a geometrical effect due to the projection of the object transverse motion along the line of sight because of its large extent on the sky, since in this case the direction of the maximum gradient is expected to be aligned with the proper motion direction.

Another possible option is that the velocity gradient is due to intrinsic rotation of the object. In this case, if the flattening of Sextans is due to intrinsic rotation, then it would be reasonable to expect the maximum gradient along the projected major axis of the object, as detected in our data. When rotation is responsible for the flattening of an axisymmetric galaxy, a simple relation holds between the true ellipticity of the galaxy and its mass weighted rotational velocity over the mass weighted velocity dispersion, v_0/σ_0 (Binney & Tremaine 1987). As for estimate of the rotational velocity we use the fitted value of the gradient at $R \sim 0.7$, the distance of the outermost stars along the major axis which cause the rotation signal in our data set: this value is $v_{\text{rot,los}} = 5.9 \text{ km s}^{-1}$ and it is likely to represent a lower limit to the maximum rotational velocity. Replacing σ_0 by the velocity dispersion measured along the line of sight, and v_0 by $v_{\text{rot,los}}$, the ratio $v_{\text{rot,los}}/\sigma_{\text{CSR}} = 0.7$ is very close to the value expected for an ‘isotropic rotator’ (0.727) of ellipticity $e = 0.35$ (as tabulated in the Binney & Merrifield 1998). This means that the shape of Sextans is consistent with being flattened by rotation, although due to the fact that Sextans velocity ellipsoid and inclination are unknown, it is possible that velocity anisotropy is also contributing to the flattening of the galaxy.

At the moment it is still difficult to build a coherent picture not only on the cause of velocity gradients in MW dSphs, but of even their presence. No significant gradient is found in Leo II (Koch et al. 2007a) where the coverage is very homogeneous. Battaglia et al. (2008b) found a significant velocity gradient along the projected major axis of the Sculptor dSph, confirmed by Walker et al. (2009a). Gradients of smaller amplitudes have also been detected in Carina and in Fornax (Walker et al. 2009a), in this case along directions close to the projected minor axis of the object. For those two objects the amplitude and direction of the gradient are consistent with being due to the transverse motion of the object along the line of sight, given their measured proper motion. However, while Carina has a very homogeneous coverage, this is not the case for Fornax, where the outer parts still await careful scrutiny. The outer parts of these objects appear to be particularly important in the measurement of velocity gradients, as shown by the case of Leo I: Mateo, Olszewski & Walker (2008) found a highly statistically significant gradient when considering only the stars located at projected distances larger than 400 arcsec, while they found no significant gradient neither when using the sample of stars at smaller projected distances, nor when considering the whole sample (which is dominated in number by the stars at $R < 400$ arcsec). Also combining data sets together may give different results: when using only their Gemini Multiobject Spectrograph (GMOS) data set Koch et al. (2007b) find no statistically significant gradient in Leo I, while when combining their GMOS data set to their Deep Imaging Multi-Object Spectrograph (DEIMOS) one the statistical significance of the detected gradient increases.

This wealth of results on the different MW dSphs shows that a coherent picture of velocity gradients as intrinsic feature in dSphs is still lacking, and so probably are data sets with both large enough statistics and homogeneous coverage to pin down values and directions of these gradients.

Velocity gradients have been detected along the projected major axis of the two isolated dSphs of the Local Group: Cetus and Tucana (Lewis et al. 2007; Fraternali et al. 2009, respectively).⁷ At the distance of Cetus and Tucana, unless of invoking three-body interactions or such (Sales et al. 2007), tidal stripping from either the MW or M31 cannot have been important, therefore it is very unlikely that the detected gradients may be attributed to tides. Also, gradients due to the transverse motion of the system are expected to be negligible due to the small extent on the sky of these objects. This would point to velocity gradients as being an intrinsic feature of these systems.

Also other spheroidal systems in the Local Group do show velocity gradients along their projected major axis. Geha et al. (2010) found significant rotation in the NGC 147 and NGC 185 dwarf elliptical galaxies (dEs). The authors calculate that the flattening of these galaxies is consistent with the amount of rotation found, although part of it may be due to anisotropy. These galaxies are dEs, not dSphs, with luminosities of the order of $10^8 L_{\odot}$, about two orders of magnitude larger than the common dSph, and one order of magnitude larger than Fornax. However, as discussed in Kormendy et al. (2009) and Tolstoy, Hill & Tosi (2009), the dEs in the Local Group (NGC 147, NGC 185 and NGC 205) share similarities with the dSphs, suggesting that these may be the high-luminosity end of the sequence.

⁷ Note though that in these two cases directions other than the major axis have not been well explored.

(iii) *Mass determination*: we have performed a Jeans analysis of the observed line-of-sight velocity dispersion profile of Sextans and find that for the best-fitting cored profiles the mass within the last measured point ranges from 3.2 to $4 \times 10^8 M_\odot$, while the mass within the last measured point for the best-fitting NFW profile is smaller, $1.9 \pm 0.6 \times 10^8 M_\odot$ but consistent within 1σ with the determination from the cored profiles. This mass range implies that Sextans contains between about 450–900 times more dark than luminous matter, in the typical range of MW dSphs.

Other authors have estimated the mass of Sextans at smaller distances from the centre. The mass that Walker et al. (2007) find within their last measured point at 1.1 kpc is $5.4 \times 10^7 M_\odot$ for a constant anisotropy and an NFW halo (with best-fitting $M_v = 3 \times 10^8 M_\odot$ and $c = 20$ derived from the concentration–virial mass relation in Jing 2000 and best-fitting $\beta = -2$). This is consistent with our model with $c = 20$, which yields $M_v = 6^{+2.5}_{-1.5} \times 10^8 M_\odot$ and $\beta = -1.7$ and $M(< 1.1 \text{ kpc}) = 5.5^{+2.3}_{-1.4} \times 10^7 M_\odot$. Note that in their analysis Walker et al. (2007) choose to fix the concentration to the virial mass according to the formula of Jing (2000) instead of exploring various concentrations for a given virial mass like in this work. It is possible that also Walker et al. (2007) data would have yielded a lower best-fitting concentration, if the correlation M_v – c was not assumed.

It has been recently shown that the determination of the DM mass within a certain distance is robust to model assumptions (e.g. Strigari et al. 2007). An interesting result has been that the mass enclosed within 0.3 (0.6 kpc) spans a narrow range of values (Gilmore et al. 2007; Strigari et al. 2007, 2008) and this could imply a minimum mass scale for the existence of luminous satellites (see also Mateo 1998, for a similar suggestion). In the determination of Strigari et al. (2007) the mass enclosed within 0.6 kpc for Sextans is $M(< 0.6 \text{ kpc}) = 0.9^{+0.4}_{-0.3} \times 10^7 M_\odot$ for a DM halo consistent with CDM predictions. For comparison, our best-fitting NFW model gives $M(< 0.6 \text{ kpc}) = 2.0 \pm 0.6 \times 10^7 M_\odot$, consistent within 2σ . Our best-fitting cored profiles instead give $M(< 0.6 \text{ kpc}) = 0.9 \pm 0.2 \times 10^7 M_\odot$ (constant β) and $M(< 0.6 \text{ kpc}) = 1.0 \pm 0.2 \times 10^7 M_\odot$, both very similar to the estimate of Strigari et al. (2007). Therefore in this case Sextans would fit in the picture of a minimum mass scale for dSphs. Note that the mass within such a small distance from the centre, while it appears to come out naturally from CDM models, is not very informative on the total DM content of the satellite: while the enclosed mass within 0.6 kpc spans one order of magnitude ($\sim 10^7$ and $\sim 10^8 M_\odot$), the total DM mass may span about three orders of magnitude, as a consequence of the lack of a tight correlation between concentration and virial mass, and of the particular (accretion and orbital) history of the satellite (Li et al. 2009).

Walker et al. (2009b, 2010) have expanded the above results to the mass enclosed within the half-light radius and also propose that all dSphs may be embedded in a DM halo of similar mass (and mass profile). The mass within the half-light radius (estimate from Walker et al. 2010, adjusted for the distance to Sextans here assumed) that we derive for the best-fitting NFW model ($c = 10$) is $M(< 0.7 \text{ kpc}) = 2.6 \pm 0.8 \times 10^7 M_\odot$, in remarkable agreement with the determination of Walker et al. (2010).⁸ The best-fitting cored DM models however give lower values, $1.4 \pm 0.2 \times 10^7 M_\odot$ ($r_c =$

3 kpc and $\beta = \text{const}$) and $1.7 \pm 0.4 \times 10^7 M_\odot$ ($r_c = 1.5 \text{ kpc}$ and $\beta = \beta_{\text{OM}}$). These estimates make Sextans fall below the ‘universal’ mass relation for dSph galaxies in Walker et al. (2010). Until degeneracies between different DM models are relieved, it is possible that universal relations between dSphs mass and other properties may change according to the adopted models.

Finally, we would like to point out that for small galactic systems such as dSphs the total mass is likely to be an important factor in determining their evolution. Indeed the depth of the potential well will influence how much of the gas and metals can be retained and therefore the subsequent star formation and chemical enrichment history from the system and how much will be expelled because of for example supernovae explosions (e.g. Revaz et al. 2009). Since outside the last measured point one can only extrapolate mass values, it will not be possible to determine total dSph masses with the current methods. However, determination as far out as possible are still important so as to provide constraints for models that aim at reproducing the detailed observed properties of stars in dSphs.

7 SUMMARY

We obtained VLT/FLAMES intermediate-resolution ($R \sim 6500$) spectroscopic observations in the near-infrared CaT region for 1036 distinct targets along the line of sight to Sextans, with magnitudes and colours broadly consistent with RGB stars. This resulted into 789 stars with S/N and error in velocity such as to produce reliable line-of-sight velocities and CaT EWs. Among those, 174 are RGB stars probable members of Sextans with line-of-sight velocities accurate to $\pm 2 \text{ km s}^{-1}$ and CaT [Fe/H] measurements accurate to $\pm 0.2 \text{ dex}$.

The vast majority of the Galactic contaminants could be weeded out from the sample using a simple 3σ kinematic cut. We refined our membership criteria by using the Mg I line at 8806.8 Å as an empirical indicator of stellar surface stellar gravity, and therefore distinguish between probable members of the dSph (RGB stars) and Galactic contaminants (most likely dwarf stars).

We used the sample of probable members to investigate the wide-field metallicity and kinematic properties of Sextans, and to perform a determination of its mass content.

Sextans is a metal-poor system, with an average [Fe/H] = -1.9 . Its stars display a wide range of metallicities, with the majority being between $-3.2 < [\text{Fe}/\text{H}] < -1.4$. A spatial variation of the metallicity properties is present, with the central parts being in average more metal rich than the outer parts. There are indications of a link with the kinematics, with the stars more metal rich than [Fe/H] = -2.2 having a lower dispersion than the stars with [Fe/H] < -2.4 .

The analysis of the radial trend of the average velocity and dispersion of Sextans stars as function of metallicity has uncovered the presence of a cold, metal-poor ([Fe/H] ~ -2.6 from CaT measurements) kinematic substructure at projected radii $R < 0.22$. This structure is consistent with being a disrupted stellar cluster. It is possible this may be the same feature observed by Kleyna et al. (2004).

Our sample of Sextans stars shows a statistically significant velocity gradient along the projected major axis of the galaxy and along an axis at PA = 191° ($8.5 \pm 3.0 \text{ km s}^{-1} \text{ deg}^{-1}$ and $7.5^{+3.4}_{-3.0} \text{ km s}^{-1} \text{ deg}^{-1}$, respectively). Given the current global observational understanding of this object it is unclear whether this gradient is due to intrinsic rotation, tidal disruption or geometrical effects. Furthermore, a better sampling of the outer parts, both in terms of spatial coverage and number statistics, would allow to place the amplitude of the

⁸ Also our other NFW models though give a very similar enclosed mass [$M(< 0.7 \text{ kpc}) = 3.0 \times 10^7 M_\odot$ for $c = 20$ and $M(< 0.7 \text{ kpc}) = 3.2 \times 10^7 M_\odot$ for $c = 35$], consequence of the degeneracy between concentration and virial mass.

velocity gradient on more secure footing and perhaps determine the overall velocity pattern throughout the face of the galaxy.

In the hypothesis of dynamical equilibrium, we performed a mass determination of Sextans, following a Jeans analysis and comparing the observed line-of-sight velocity dispersion profile to the predictions for cored and cuspy DM models. Sextans appears to be a very DM dominated object, with a mass within 2.3 kpc of $2-4 \times 10^8 M_{\odot}$, giving a dynamical mass-to-light ratio between 460 and $920 (M/L)_{V, \odot}$. Within the explored DM models and velocity anisotropy profiles, the best fits are given by cored profiles with large core radius and mildly radial anisotropy. However also a NFW profile with mildly tangential anisotropy gives a very good representation of the data; the concentration of the favoured NFW is $c = 10$ somewhat lower for what expected for galaxies in the mass range of Sextans when using the virial mass–concentration relation of Jing (2000).

ACKNOWLEDGMENTS

GB and PP are grateful to the Kapteyn Astronomical Institute for hospitality and financial support during part of this work. GB thanks F. Fraternali for useful suggestions. The authors acknowledge E. Starkenburg for kindly running preliminary models regarding the Mg I line. Financial support by the European Research Council has been provided to AH in the form of SZG-GALACTICA, #240271.

REFERENCES

- Aoki W. et al., 2009, *A&A*, 502, 569
 Battaglia G., 2007, PhD thesis, Kapteyn Astronomical Institute, Univ. Groningen
 Battaglia G. et al., 2006, *A&A*, 459, 423
 Battaglia G., Irwin M., Tolstoy E., Hill V., Helmi A., Letarte B., Jablonka P., 2008a, *MNRAS*, 383, 183
 Battaglia G., Helmi A., Tolstoy E., Irwin M., Hill V., Jablonka P., 2008b, *ApJ*, 681, L13
 Bellazzini M., Ferraro F. R., Pancino E., 2001, *MNRAS*, 327, L15
 Binney J., Mamon G. A., 1982, *MNRAS*, 200, 361
 Binney J., Merrifield M., 1998, *Galactic Astronomy*. Princeton Univ. Press, Princeton, NJ
 Binney J., Tremaine S., 1987, *Galactic Dynamics*. Princeton Univ. Press, Princeton, NJ
 Blecha A., North P., Royer F., Simond G., 2003, *VLT-SPE-OGL-13730-0040*
 Bullock J. S., Kolatt T. S., Sigad Y., Somerville R. S., Kravtsov A. V., Klypin A. A., Primack J. R., Dekel A., 2001, *MNRAS*, 321, 559
 Carretta E., Gratton R. G., 1997, *A&AS*, 121, 95
 Cole A. A., Smecker-Hane T. A., Tolstoy E., Bosler T. L., Gallagher J. S., 2004, *MNRAS*, 347, 367
 Da Costa G. S., Hatzidimitriou D., Irwin M. J., McMahon R. G., 1991, *MNRAS*, 249, 473
 Dehnen W., Binney J. J., 1998, *MNRAS*, 298, 387
 Faria D., Feltzing S., Lundström I., Gilmore G., Wahlgren G. M., Ardeberg A., Linde P., 2007, *A&A*, 465, 357
 Fraternali F., Tolstoy E., Irwin M. J., Cole A. A., 2009, *A&A*, 499, 121
 Geha M., van der Marel R. P., Guhathakurta P., Gilbert K. M., Kalirai J., Kirby E. N., 2010, *ApJ*, 711, 361
 Geisler D., Sarajedini A., 1996, in Morrison H. L., Sarajedini A., eds, *ASP Conf. Ser. Vol. 92, Formation of the Galactic Halo: Inside and Out*. Astron. Soc. Pac., San Francisco, p. 524
 Gilmore G., Wilkinson M. I., Wyse R. F. G., Kleyna J. T., Koch A., Evans N. W., Grebel E. K., 2007, *ApJ*, 663, 948
 Gullieuszk M., Held E. V., Saviane I., Rizzi L., 2009, *A&A*, 500, 735
 Harbeck D. et al., 2001, *AJ*, 122, 3092
 Hargreaves J. C., Gilmore G., Irwin M. J., Carter D., 1994, *MNRAS*, 269, 957
 Helmi A. et al., 2006, *ApJ*, 651, L121
 Hoaglin D. C., Mosteller F., Tukey J. W., eds, 1983, *Understanding Robust and Exploratory Data Analysis*. Wiley, New York
 Illingworth G., 1976, *ApJ*, 204, 73
 Irwin M., Hatzidimitriou D., 1995, *MNRAS*, 277, 1354
 Irwin M. J., Bunclark P. S., Bridgeland M. T., McMahon R. G., 1990, *MNRAS*, 244, 16p
 Jing Y. P., 2000, *ApJ*, 535, 30
 Kleyna J. T., Wilkinson M. I., Gilmore G., Evans N. W., 2003, *ApJ*, 588, L21
 Kleyna J. T., Wilkinson M. I., Evans N. W., Gilmore G., 2004, *MNRAS*, 354, L66
 Klypin A., Zhao H., Somerville R. S., 2002, *ApJ*, 573, 597
 Koch A., Grebel E. K., Wyse R. F. G., Kleyna J. T., Wilkinson M. I., Harbeck D. R., Gilmore G. F., Evans N. W., 2006, *AJ*, 131, 895
 Koch A., Grebel E. K., Kleyna J. T., Wilkinson M. I., Harbeck D. R., Gilmore G. F., Wyse R. F. G., Evans N. W., 2007a, *AJ*, 133, 270
 Koch A., Wilkinson M. I., Kleyna J. T., Gilmore G. F., Grebel E. K., Mackey A. D., Evans N. W., Wyse R. F. G., 2007b, *ApJ*, 657, 241
 Kormendy J., Fisher D. B., Cornell M. E., Bender R., 2009, *ApJS*, 182, 216
 Lee M. G. et al., 2003, *AJ*, 126, 2840
 Letarte B., Hill V., Jablonka P., Tolstoy E., François P., Meylan G., 2006, *A&A*, 453, 547
 Lewis G. F., Ibata R. A., Chapman S. C., McConnachie A., Irwin M. J., Tolstoy E., Tanvir N. R., 2007, *MNRAS*, 375, 1364
 Li Y., Helmi A., De Lucia G., Stoehr F., 2009, *MNRAS*, 397, L87
 Łokas E. L., 2009, *MNRAS*, 394, L102
 Łokas E. L., Mamon G. A., Prada F., 2005, *MNRAS*, 363, 918
 Mamon G. A., Łokas E. L., 2005, *MNRAS*, 363, 705
 Mateo M. L., 1998, *ARA&A*, 36, 435
 Mateo M., Nemeč J., Irwin M., McMahon R., 1991, *AJ*, 101, 892
 Mateo M., Fischer P., Krzemiński W., 1995, *AJ*, 110, 2166
 Mateo M., Olszewski E. W., Walker M. G., 2008, *ApJ*, 675, 201
 Merritt D., 1985, *MNRAS*, 214, 25p
 Muñoz R. R., Majewski S. R., Johnston K. V., 2008, *ApJ*, 679, 346
 Navarro J. F., Frenk C. S., White S. D. M., 1996, *ApJ*, 462, 563
 Navarro J. F., Frenk C. S., White S. D. M., 1997, *ApJ*, 490, 493
 Oh K. S., Lin D. N. C., Aarseth S. J., 1995, *ApJ*, 442, 142
 Okamoto S. et al., 2008, in Kodama T., Yamada T., Aoki K., eds, *ASP Conf. Ser. Vol. 399, The Star Formation History and Stellar Population Structures in the Sextans Dwarf Spheroidal Galaxy*. Astron. Soc. Pac., San Francisco, p. 469
 Osipkov L. P., 1979, *Soviet Astron. Lett.*, 5, 42
 Pasquini L. et al., 2002, *Messenger*, 110, 1
 Pryor C., McClure R. D., Fletcher J. M., Hesser J. E., 1988, in Davis Philip A. G., Grindlay J. E., eds, *Proc. IAU Symp. Vol. 126, Globular Cluster Systems in Galaxies*. Reidel, Dordrecht, p. 661
 Revaz Y. et al., 2009, *A&A*, 501, 189
 Robin A. C., Reylé C., Derrière S., Picaud S., 2003, *A&A*, 409, 523
 Rutledge G. A., Hesser J. E., Stetson P. B., Mateo M., Simard L., Bolte M., Friel E. D., Copin Y., 1997, *PASP*, 109, 883
 Sales L. V., Navarro J. F., Abadi M. G., Steinmetz M., 2007, *MNRAS*, 379, 1475
 Schlegel D. J., Finkbeiner D. P., Davis M., 1998, *ApJ*, 500, 525
 Shetrone M. D., Côté P., Sargent W. L. W., 2001, *ApJ*, 548, 592
 Starkenburg E. et al., 2010, *A&A*, 513, A34
 Strigari L. E., 2010, *Advances Astron.*, 2010, 11
 Strigari L. E., Bullock J. S., Kaplinghat M., Diemand J., Kuhlen M., Madau P., 2007, *ApJ*, 669, 676
 Strigari L. E., Bullock J. S., Kaplinghat M., Simon J. D., Geha M., Willman B., Walker M. G., 2008, *Nat*, 454, 1096
 Suntzeff N. B., Mateo M., Terndrup D. M., Olszewski E. W., Geisler D., Weller W., 1993, *ApJ*, 418, 208
 Swaters R. A., Madore B. F., Trewheella M., 2000, *ApJ*, 531, L107
 Tafelmeyer M. et al., 2010, *arXiv:1008.3721*
 Tolstoy E. et al., 2004, *ApJ*, 617, L119
 Tolstoy E., Hill V., Tosi M., 2009, *ARA&A*, 47, 371
 van den Bergh S., 2006, *AJ*, 131, 304

- Walker M. G., Mateo M., Olszewski E. W., Pal J. K., Sen B., Woodroffe M., 2006, *ApJ*, 642, L41
- Walker M. G., Mateo M., Olszewski E. W., Gnedin O. Y., Wang X., Sen B., Woodroffe M., 2007, *ApJ*, 667, L53
- Walker M. G., Mateo M., Olszewski E. W., 2008, *ApJ*, 688, L75
- Walker M. G., Mateo M., Olszewski E. W., 2009a, *AJ*, 137, 3100
- Walker M. G., Mateo M., Olszewski E. W., Peñarrubia J., Wyn Evans N., Gilmore G., 2009b, *ApJ*, 704, 1274
- Walker M. G., Mateo M., Olszewski E. W., Peñarrubia J., Wyn Evans N., Gilmore G., 2010, *ApJ*, 710, 886
- Wechsler R. H., Bullock J. S., Primack J. R., Kravtsov A. V., Dekel A., 2002, *ApJ*, 568, 52

APPENDIX A: COMPARISON WITH WALKER ET AL. (2009)

We compare our data set of objects with $S/N \geq 10$ and velocity errors $\leq 5 \text{ km s}^{-1}$ to the recent data set of Walker et al. (2009a) consisting of spectroscopic observations of 947 distinct targets along the line of sight to Sextans acquired with the Michigan/MIKE Fiber System ($R = 20\,000\text{--}25\,000$). These spectra cover the wavelength range $5140\text{--}5180 \text{ \AA}$ including the magnesium triplet absorption feature which the authors use, together with calibrating globular clusters, to provide an estimate of $[\text{Fe}/\text{H}]$ for the individual stars.

A1 Velocities

There are 141 overlapping individual stars with velocity determinations between our and Walker et al. (2009a) samples, including probable members and non-members. In Fig. A1 (left) we compare the line-of-sight velocities for the stars overlapping between the two samples.

The agreement between the velocity determinations in the two data sets is good: the weighted average velocity difference between the two samples is $1.3 \pm 1.3 \text{ km s}^{-1}$, with a scaled MAD

of 3.8 km s^{-1} (corresponding to about an average velocity error of 2.5 km s^{-1} in each of the two data sets) and 1.4 for the distribution of velocity differences normalized by the errors. Overall the agreement is good, except for five stars, which have velocities consistent with membership to Sextans in our sample but heliocentric velocities below 20 km s^{-1} in the Walker et al. (2009a) sample, which would classify them as clearly MW stars: the velocities of these differ by about $250\text{--}300 \text{ km s}^{-1}$ between the two samples. All these stars have very reasonable S/N in our data and visual examination of the spectra of these five stars with discrepant velocities does not reveal any problem with the spectrum (i.e. CaT is in general visible enough to allow a reasonable velocity estimation with our routine). We find it unlikely that these may all be binary stars, but the reason for this discrepancy remains unclear.

Excluding these five stars does not significantly alter the quality of the comparison between the two samples, bringing some improvement in the average velocity difference between the two samples ($0.41 \pm 0.44 \text{ km s}^{-1}$), while the scaled MAD remains almost unchanged.

A2 Metallicities

Since the $[\text{Fe}/\text{H}]$ calibrations in both studies are based on different spectral features, a comparison between the $[\text{Fe}/\text{H}]$ determinations of the individual stars is expected to be meaningful only when considering probable Sextans members, and not for the MW contaminants for which the luminosity correction for the dwarf stars is likely to be incorrect and different in the two studies. Walker et al. (2009a) derive $[\text{Fe}/\text{H}]$ measurements from an Mg index and place them on the Carretta & Gratton (1997) scale (their equation 7). The calibration of the spectral indexes to a $[\text{Fe}/\text{H}]$ scale requires a correction for the V magnitude of the stars, therefore, the authors provided $[\text{Fe}/\text{H}]$ values only for those Sextans stars in common between their sample and the photometric study of Lee et al. (2003),

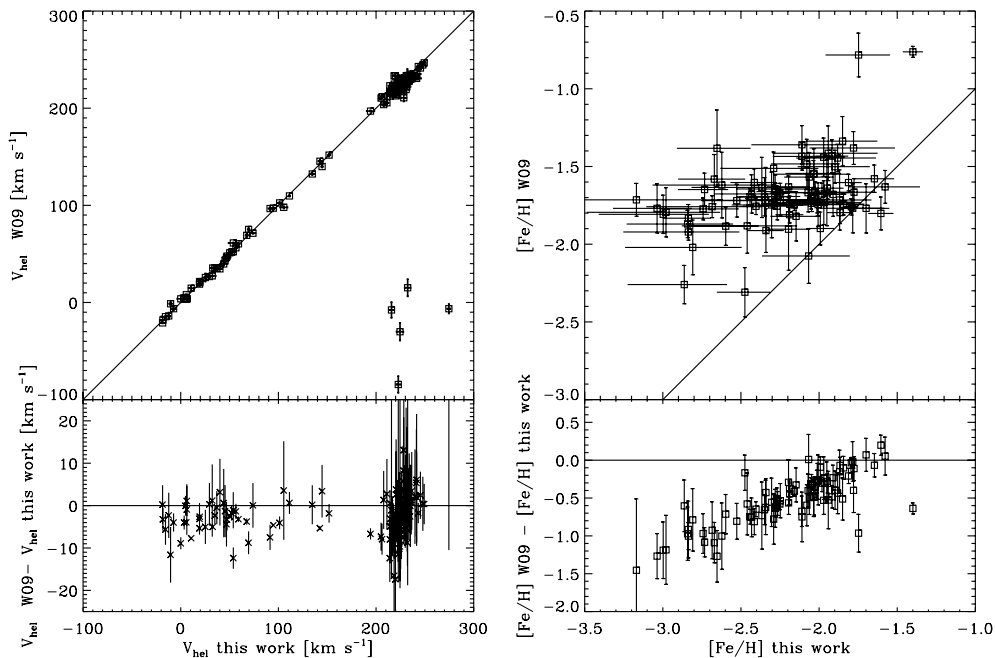


Figure A1. Comparison between overlapping stars between this work and Walker et al. (2009a). The comparison for the velocity determinations is shown in the left-hand panels (134 stars, both probable members and non-members), and for the $[\text{Fe}/\text{H}]$ values in the right-hand panels (94 stars, only probable members). The top panels show the direct comparison, with the solid line indicating the one-to-one relation; the bottom panels show the differences among the determinations as a function of the quantities derived in this work, with the solid line indicating a null difference.

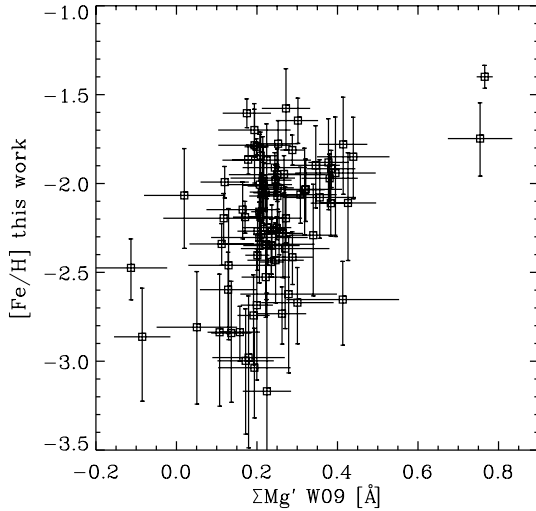


Figure A2. $[\text{Fe}/\text{H}]$ values as determined in this work against determinations of the Mg spectral index from Walker et al. (2009a) for 94 Sextans probable members which overlap between the two samples. Note the large range of $[\text{Fe}/\text{H}]$ values corresponding to a narrow range in spectral index values.

using the V magnitudes derived in the latter work. This would result in 50 probable Sextans members with $[\text{Fe}/\text{H}]$ estimates in common between the two studies. In order to increase the number of stars available for comparison with our sample, we check that the V magnitudes obtained from our photometry compares well to the determinations of Lee et al. (2003) for the same stars, and then use our V magnitudes for those stars in common between our sample and Walker's but that did not have determinations from Lee et al. (2003): this gives an additional 44 probable members in common between the two samples. The results of the comparison are shown

in the right-hand panel of Fig. A1: in general the determinations from W09 yield higher values of $[\text{Fe}/\text{H}]$ (more metal rich) and the $[\text{Fe}/\text{H}]$ distribution appears much narrower. This effect was also highlighted by Walker et al. (2009a) and the authors themselves advise against using the determinations from the Mg index as absolute values. The authors suggest that the Mg spectral index could be used as a relative indicator of metallicity. In Fig. A1 (right) we show that the metallicities from the Mg spectral index correspond to a narrower range than the more reliable CaT measurements, suggesting a limited use of the Mg index also for relative measurements. It appears also not possible to carry out a reliable calibration between $[\text{Fe}/\text{H}]$ estimates from CaT and from Mg index because of the large scatter between the two quantities (Fig. A2).

The fact that the Mg index is not a good indicator of $[\text{Fe}/\text{H}]$ prevents us from combining our sample of metallicities with those of Walker et al. (2009a). However, such a merged data set would be most helpful to considerably increase the size and coverage of both works.

SUPPORTING INFORMATION

Additional Supporting Information may be found in the online version of this article:

Table 4. The relevant data for the stars in Sextans observed with VLT/FLAMES that passed our membership criteria.

Please note: Wiley-Blackwell are not responsible for the content or functionality of any supporting materials supplied by the authors. Any queries (other than missing material) should be directed to the corresponding author for the article.

This paper has been typeset from a $\text{T}_{\text{E}}\text{X}/\text{L}^{\text{A}}\text{T}_{\text{E}}\text{X}$ file prepared by the author.